A petrologic anomaly accompanying outboard earthquakes beneath Fiji-Tonga: Corresponding evidence from broadband *P* and *S* waveforms

Michael R. Brudzinski[1] and Wang-Ping Chen

Department of Geology, University of Illinois at Urbana-Champaign, Urbana, Illinois, USA

[1] Using high-resolution, triplicate body waveforms, we investigate strong lateral variations in *P* and *SH* wave speeds (V_P and V_S) beneath the Tonga subduction zone where cold lithosphere is subducting rapidly at 200 mm yr^{-1}. Under these conditions, the lack of prominent anomalies of high V_P and V_S in the lower mantle implies that a large amount of recently subducted material remains above the lower mantle. This inference is also evident from a subhorizontal swath of outboard earthquakes in the transition zone that is up to 1000 km away from the Wadati-Benioff zone. Beneath the back arc, we find a sharp, east-west trending demarcation north of which outboard earthquakes occur and V_P and V_S abruptly drop by ∼3%. Thus the effect of cold temperature to raise V_P and V_S, as indicated by the presence of outboard earthquakes, must be counteracted by petrologic variations. We interpret that outboard earthquakes occur where impounding of subducted metastable olivine or volatiles reduces seismic wave speeds and triggers deep earthquakes. Considering the density of these candidates and the strong effect of partial melt on V_S, volatiles in the form of hydrous phases or melt induced by dehydration are not consistent with observed reductions in V_P and V_S. Meanwhile, metastable olivine remains a viable candidate. As a cold slab passes below the 410-km discontinuity, olivine becomes metastable and makes the tip of the slab buoyant. Such a mechanism could explain why the leading end of a fast subducting slab may be successively sequestered in the transition zone.   *INDEX TERMS:* 1025 Geochemistry: Composition of the mantle; 7203 Seismology: Body wave propagation; 8120 Tectonophysics: Dynamics of lithosphere and mantle—general; 7218 Seismology: Lithosphere and upper mantle; *KEYWORDS:* petrologic anomaly, mantle structure, seismic wave speeds, waveform modeling, outboard earthquakes, Fiji-Tonga

1. Introduction

[2] The interaction between subducted lithosphere and the transition zone of the mantle is a key issue in geodynamics. In particular, the amount of slab penetration into the lower mantle controls the rate of heat and mass transfer between the upper and the lower mantle [e.g., *Lay*, 1994; *Silver et al.*, 1988]. These processes are central to understanding thermal convection and chemical mixing of the mantle, including the continual search for a primordial mantle [e.g., *Albaréde and van der Hilst*, 1999; *Chen and Frey*, 1983; *Kellogg et al.*, 1999; *Vidale et al.*, 2001].

[3] The Tonga subduction zone is a natural laboratory for studying mantle dynamics because large amounts of old, cold slab have been rapidly subducting in the past 50–100 Myr [e.g., *Chase*, 1971; *Lithgow-Bertelloni and Richards*, 1998; *Richards and Engebretson*, 1992]. Presently, the rate of subduction exceeds 200 ± 40 mm yr^{-1} [*Bevis et al.*, 1995] (Figure 1). Considering the old age of the Pacific lithosphere being subducted and the extremely fast rate of convergence, subducted material beneath Tonga should have caused the most prominent thermal anomaly in the mantle [e.g., *McKenzie*, 1970; *Stein and Stein*, 1996].

[4] However, global travel time tomography showed only moderate anomalies of fast *P* and *S* wave speeds (V_P and V_S) in the lower mantle along the Tonga subduction zone [e.g., *Grand et al.*, 1997; *van der Hilst et al.*, 1997], consistent with earlier analysis of travel times that indicated a modest anomaly extending down to no more than 900 km in depth [*Fischer et al.*, 1991]. Thus a large amount of subducted material must have remained above the lower mantle [*Chen and Brudzinski*, 2001] (hereinafter referred to as CB2001). Questions naturally arise as to how and why cold slab is being sequestered above the lower mantle in Tonga. In particular, one or more processes must somehow counteract the negative buoyancy of subducted material.

[5] It is a basic tenet of plate tectonics that earthquakes deeper than about 100 km occur in the cold interior of

---

[1]Now at Department of Geology and Geophysics, University of Wisconsin-Madison, Madison, Wisconsin, USA.
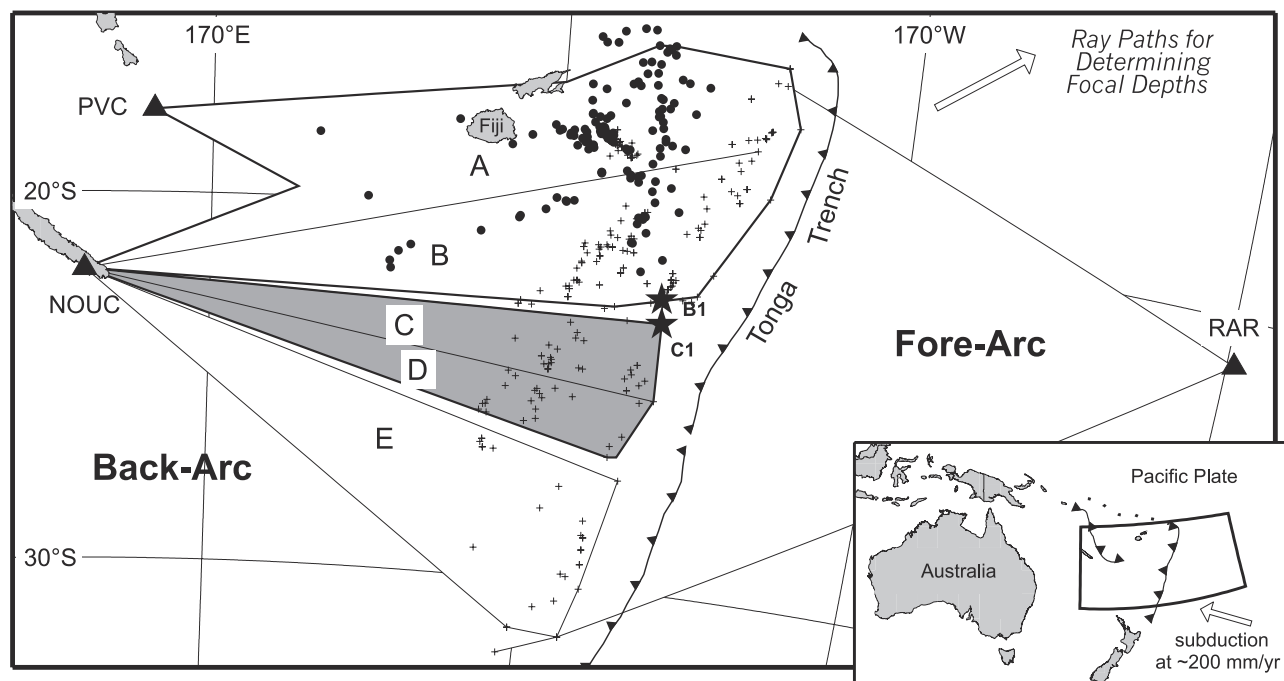
Figure 1. Map showing azimuthal sectors (A–E and forearc) that characterize lateral variations in V_P and V_S. Two distinct types of deep earthquakes occur in this region. In addition to seismicity forming the familiar, inclined Wadati-Benioff zone (WBZ, epicenters plotted as crosses), there is an unusual, subhorizontal group of outboard earthquakes (solid circles) that occur in the transition zone of the mantle, up to 1000 km away from the WBZ. Labels A–E mark the average location where ray paths used in our experiment bottom near the mantle transition zone. Thus models shown in Figure 2 are most sensitive to V_P and V_S near these locations. Notice that in the transition zone, regions of high V_P and V_S are restricted to sectors C and D (gray shading), terminating abruptly northward where outboard earthquakes occur in sectors B and A. For seismicity, we plot only large ($m_b \geq 5$) outboard earthquakes that occurred between 1964 and 1999 [CB2001] and deep earthquakes (≥ 50 km) within the WBZ whose waveforms recorded at broadband stations NOUC, PVC and RAR (solid triangles) are used in this study (Appendix C). For each event used, its focal depth is estimated from the timing of the pP phase recorded at teleseismic stations along azimuths that span the forearc, where V_P and V_S are laterally homogeneous. B1 and C1 mark epicenters of events whose waveforms are discussed in detail (Figures 3 and 4). The inset shows the overall tectonic setting of the Tonga subduction zone.

subducted lithosphere [e.g., *Isacks and Molnar*, 1971; *Isacks et al.*, 1968; *Molnar et al.*, 1979]. Otherwise, deep earthquakes would not be restricted to zones of recent convergence. So in the transition zone of the mantle, deep earthquakes also delineate the distribution of recently subducted material.

[6] Specific mechanisms that have been proposed for deep earthquakes include transformational faulting of metastable olivine [e.g., *Green and Burnley*, 1989; *Kirby et al.*, 1991] and dehydration or amorphization of hydrous phases [e.g., *Meade and Jeanloz*, 1991]. Both hypotheses involve the presence of compositional or mineralogical anomalies that are characterized by low seismic wave speeds in the mantle transition zone. In principle, such a feature is detectable by carefully investigating the distribution of seismic wave speeds in regions where dense seismicity occurs in the mantle.

[7] Seismicity along the Tonga subduction zone is most active, accounting for about half of all deep earthquakes in the world [e.g., *Frohlich*, 1989]. A unique feature is a subhorizontal swath of deep (>300 km) outboard earth-

quakes that extends up to one thousand kilometers farther to the west of the Wadati-Benioff zone (WBZ, equivalent to the trace of actively subducting lithosphere) [e.g., *Hamburger and Isacks*, 1987; *Okal and Kirby*, 1998] (Figure 1). The wide extent of the outboard earthquakes provides a favorable configuration for modeling high-resolution, broadband body waveforms in order to precisely determine seismic wave speeds in the earthquake-generating (seismogenic) material [*Brudzinski and Chen*, 2000] (hereinafter referred to as BC2000).

[8] In the transition zone of the mantle, seismic wave speeds are mainly a function of temperature and petrology. In the source region of outboard earthquakes, seismicity independently indicates cold temperature, a condition expected to raise both V_P and V_S. Contrary to this expectation, however, BC2000 found that regions of high V_P occur immediately to the south of outboard earthquakes, while the seismogenic zone itself is characterized by moderate values of V_P that are similar to those beneath the forearc, a region yet to be affected by subduction. These observations indicate that outboard earthquakes must be

accompanied by a petrologic anomaly, such as volatiles or metastable polymorphs of mantle minerals, which counteracts the thermal effect on V_P.

[9] In the current study, we report new findings based on broadband waveforms of horizontally polarized shear waves (SH). In addition, we expand and refine our previous results of V_P so now both P and SH ray paths densely cover the entire seismogenic zone of outboard earthquakes. We shall show corresponding evidence of V_P and V_S that points to the lack of high seismic wave speeds in the source zone of outboard earthquakes. When combined with results of V_P, the newly available observations of V_S place tight constraints on the nature of this petrologic anomaly that must both reduce seismic wave speeds and be able to trigger deep earthquakes.

[10] Finally, we shall investigate how low density of various candidates for the petrologic anomaly affects subduction. In particular, we discuss an intriguing effect of metastable olivine that may cause the tip of a fast subducting slab to become buoyant in the transition zone of the mantle. This effect not only provides a simple explanation for the subhorizontal configuration of outboard seismicity but also has implications for sequestering a large amount of cold slab above the lower mantle.

2. Data and Analysis

[11] We use digital data from three permanent, broadband stations flanking the Tonga subduction zone: Port Laguerre (NOUC) and Port Vila (PVC) in the back arc, and Rarotonga (RAR) in the forearc (Figure 1). We examine seismograms from large- to moderate-sized ($m_b \geq 5.0$) events that have occurred since the inception of broadband recording at each station (circa 1990) up to 1999. We focus only on events within epicentral distances of approximately $10-20°$, so these waveforms are primarily sensitive to V_P and V_S at depths near the mantle transition zone. In addition, each event must have produced enough data at teleseismic distances for us to precisely determine its focal depth and source time function. In all, we use 208 earthquakes, ranging in depths from 48 to 656 km along the Tonga WBZ (Table C1, Appendix C[1]). We use these events to construct a sequence of seismic profiles in the same manner as BC2000.

[12] In each profile, variations in epicentral distances and focal depths provide ray paths that sample different depths. The basic principle is similar to conventional seismic profiling in which rays traveling longer distances sample greater depths in the mantle. Moreover, deep earthquakes offer several additional advantages. First, a deep earthquake has a greater effective aperture than a shallow event at the same epicentral distance. To visualize this effect, one can trace a ray backward from the station, passing through the hypocenter, until one reaches the free surface at a greater distance. Second, rays from deep earthquakes are particularly sensitive to V_P and V_S deep in the mantle. Soon after leaving the source region, these rays travel subhorizontally within the

transition zone or the lower mantle (event 2 in Figure A1) and pass the upper mantle only once near the station (Figure A1). Third, while triplicate arrivals are strong from a source located above a discontinuity (event 1 in Figure A1), such arrivals would be completely absent for a source located just below the discontinuity (event 2 in Figure A1). Notice that the latter case signifies the crossing of a discontinuity and naturally isolates signals from another discontinuity below.

[13] In the following paragraphs, we briefly review the overall scheme of data processing and analysis, with additional details discussed in Appendix A and BC2000. We begin our analysis in the forearc, where subducted lithosphere is yet to interact with the transition zone. First, we construct an east-west profile covering a narrow range of azimuths near $90°$. We then test the resulting model of radially varying V_P and V_S against data from an increasing range of azimuths to detect any lateral variations of V_P and V_S. As it turns out, the forearc region is laterally homogeneous, and a single model is sufficient to explain all observed waveforms and travel times (Figure 1).

[14] We then use a similar "fan shot" approach in the back arc. First, we seek the simplest model of V_P and V_S that explains all waveforms and travel times within a narrow sector of back azimuths. Then the range of back azimuths is expanded to include neighboring paths until a single model is no longer adequate for all observed waveforms and travel times. This process defines the boundaries of each sector within which waveforms can be approximated by the same model. Typically, the boundary between sectors can be narrowed down to a width of ~20 km in the north-south direction (Figure 1). There is very little ambiguity in distinguishing different sectors, as variations in V_P and V_S among sectors are larger than any internal variations within each sector. We find that up to five sectors are sufficient to describe strong lateral variations in the back arc (sectors A$-$E, Figure 1) and there is no justification for using a more complex scheme of models.

[15] To facilitate direct comparisons of waveforms from different earthquakes (source normalization), we deconvolve each observed waveform with an appropriate reference signal. For each earthquake, the reference signal is a P or SH wave train recorded at approximately the same azimuth as the waveform of interest but at a teleseismic station. At teleseismic distances ($30-90°$), complications due to triplications in the upper mantle and to phases interacting with the core are minimal. As such, the reference signal is a good approximation of the source time function, including the effect of a finite source along that particular azimuth. For SH waveforms, we use a teleseismic SH wave train and/or an appropriately attenuated teleseismic P wave train in deconvolution [e.g., *Glennon and Chen*, 1993; *Zhou et al.*, 2000]. When the noise level is low, the two reference signals give identical results.

[16] During deconvolution, we apply a zero-phase, bandpass filter so in the resulting seismogram, the onset of an arrival from the forward branch of a triplication corresponds to the peak of an acausal, symmetric wavelet. For comparison, visually picked first arrivals are also plotted in Figures $3-5$ (in sections 3.1 and 3.2), A2$-$A9 (in Appendix A), and B1$-$B2 (in Appendix B). When the signal-to-noise ratios of both regional and teleseismic data are high, and when the source time function is simple, deconvolution results in a

---

[1] Auxiliary Table C1 is available via Web browser or via Anonymous FTP from ftp://agu.org/apend/jb/2002JB002012/ (Username = "anonymous", Password = "guest"); subdirectories in the ftp site are arranged by paper number. Information on searching and submitting electronic supplements is found at http://www.agu.org/pubs/esupp_about.html.
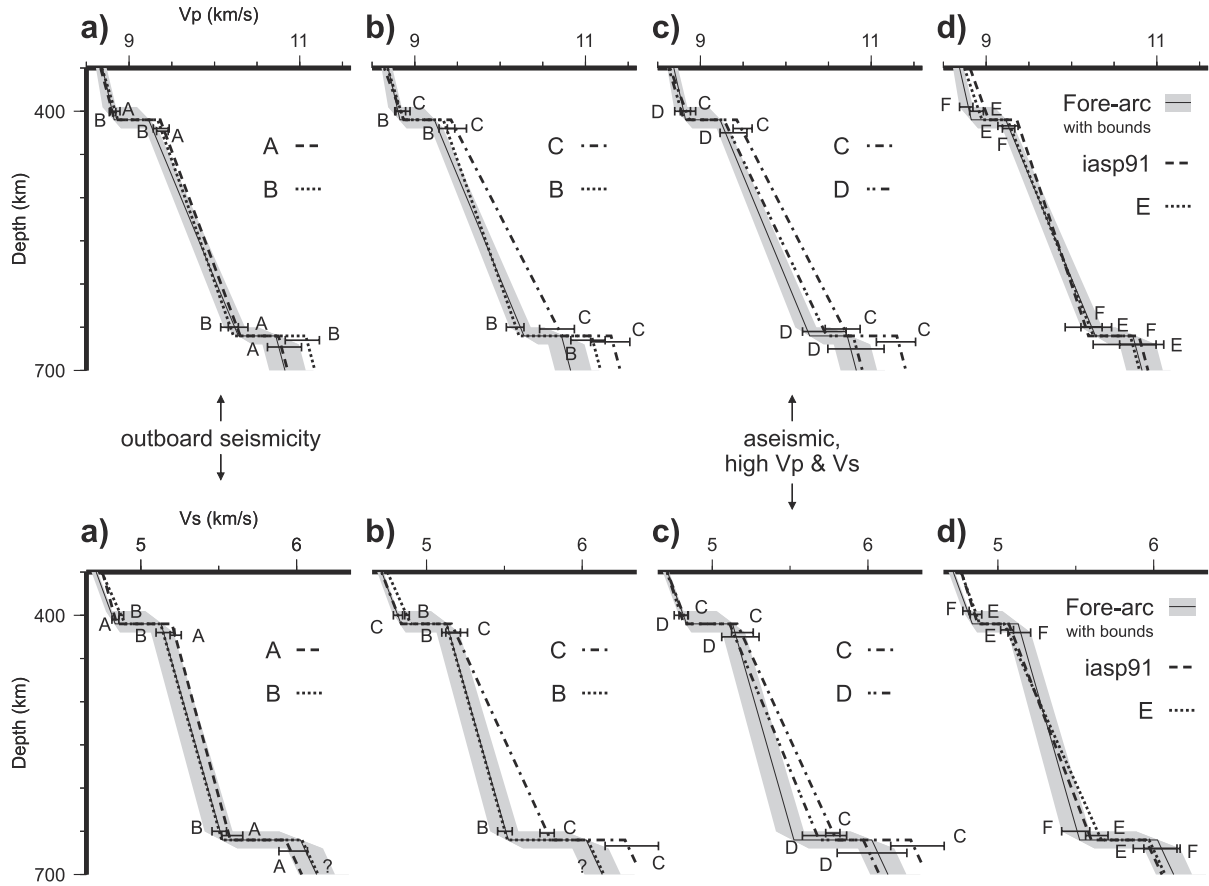
Figure 2. Comparisons of (top) V_P and (bottom) V_S among sectors. The width of each horizontal error bar indicates the range of acceptable V, while the vertical position of the bar marks the upper or lower bound on the depth of a seismic discontinuity. Error bars show generous estimates of uncertainty by attributing misfits in absolute timing entirely to fluctuations in V_P and V_S within a sector. Nevertheless, any acceptable model within the maximum estimate of errors must still preserve the overall shape of how V_P and V_S changes over depth. For instance, the lowest possible V_P and V_S in the transition zone and the highest possible V_P and V_S in the lower mantle as depicted are not an acceptable combination (Tables A1 and A2).

wave train containing clear arrivals that are then modeled by synthetic seismograms. In addition, the timing of all impulsive first arrivals recorded at regional distances is used to constrain models for V_P and V_S.

[17] We calculate synthetic seismograms using the WKBJ algorithm [*Chapman*, 1978; *Chapman et al.*, 1988], with fault plane solutions from the Harvard CMT catalog [*Dziewonski et al.*, 1981] and relocated epicenters of *Engdahl et al.* [1998]. For each earthquake, we independently determine its precise focal depth from travel times and waveforms of the phase *pP* recorded at teleseismic distances. For this purpose, we use data along azimuths that span only the forearc where we jointly determined V_P and focal depths in an iterative manner [BC2000].

[18] We search the model space via forward modeling to determine best fitting models of V_P and V_S for each sector. The best fitting model minimizes misfits between observed and synthetic seismograms in relative timing, relative amplitudes, and absolute timing. Within each sector, our data constrain V_P and V_S at depths of approximately 300–700 km, including the gradient of V_P and V_S with respect to depth in the transition zone, the increases in V_P and V_S across both the 410- and 660-km discontinuities, and the depths of these discontinuities. Each of these parameters is subject to a

priori constraints, limited by extreme values summarized by *Kennett* [1993]. To estimate error bounds of these parameters, we explore the model space by perturbing the best fitting models until synthetic seismograms show large misfits in relative amplitude, relative timing, or absolute timing.

[19] We reject models if (1) they produce misfits in relative timing that are larger than two standard deviations of those from the best fitting model, or (2) the predicted amplitude ratio between any two arrivals is off by more than a factor of two. In practice, the criterion for misfit in relative timing is 0.5 s for *P* and 0.9 s for *SH* (Appendix A), consistent with V_P/V_S of ~1.8. The misfits are likely to be the effect of either random errors in epicenter location or slight variations in V_P and V_S within a sector. Either way, variations in V_P and V_S between sectors are beyond conceivable variation within sectors (Figure 2). To this end, relative timing and amplitudes are sufficient to distinguish different sectors; absolute timing is not required for this purpose.

[20] For the best fitting model of any single sector, the mean misfit in absolute timing of first arrivals is close to zero (<0.1 s), with a standard deviation of approximately ±1.0 s for *P* waves. This pattern in absolute timing resembles random errors due to mislocation of epicenters by approximately ±10 km. Such a mislocation has some

secondary effects on relative timing (up to ±0.3 s) and relative amplitudes (up to ±30%). Since one can never rule out possible errors in location and origin time of any earthquake, we consider two extreme cases. In the first case, fluctuations in absolute timing are attributed to mislocation alone, not contributing to uncertainties in V_P and V_S. The result is a minimal estimate of errors in V_P and V_S. In the second case, fluctuations in absolute timing are assumed to solely reflect variations in V_P and V_S, resulting in a maximal estimate of errors in our models. The actual bounds on V_P and V_S probably lie between these two extreme cases. The final error bounds we report use the maximal estimate of errors (Figure 2).

3.   Results

[21]   Overall, spatial variations in V_P and V_S are similar and mainly occur in the transition zone of the mantle. Prominent anomalies of high V_P and V_S appear beneath the central portion of the back arc (sectors C and D, Figure 2). The northern edge of high V_P and V_S abuts the southern terminus of outboard earthquakes (sectors A and B, Figure 1) where V_P and V_S drop by about 3% to values close to those beneath the forearc (Figure 2), even though one expects high V_P and V_S associated with cold temperatures in the seismogenic zone. The southernmost portion of the back-arc region, sector E, is also characterized by V_P and V_S that are close to the iasp91 model for the average Earth [*Kennett and Engdahl*, 1991] (Figure 2d).

[22]   For V_P, using refined locations of epicenters [*Engdahl et al.*, 1998] and an expanded set of waveforms in the current study, the results generally corroborate our previous report [BC2000]. Consequently, we emphasize new, corresponding evidence from V_S as we focus on key features in our models and on illustrating the resolution of our analysis in this section. Additional evidence from waveforms and specifics of models are presented in Appendix A.

3.1.   Sharp Boundary in V_P and V_S at Southern Terminus of Outboard Earthquakes

[23]   Using waveforms from events that straddle the southern termination of outboard earthquakes (events B1 and C1 in Figure 1), we find that V_P and V_S are on average 3% faster immediately south of the outboard earthquakes (Figures 3 and 4). In sector C, high V_S is evident from the *SH* waveform of event C1 (Figure 3b), as the ray diving into the transition zone (C'A) arrives ∼3 s earlier than those turning above the 410-km discontinuity (cusp B'). These arrivals are easily distinguished from each other based on the phase shift of arrivals from cusp B'. Notice that the model for sector B predicts C'A to arrive close to cusp B' (dotted trace, Figure 3b), reflecting a slow traveling C'A phase in the transition zone of sector B.

[24]   Similarly, the *SH* waveform of event B1 directly indicates low V_S in the transition zone of sector B (Figure 3a). Synthetic seismograms from such a model can accurately match arrivals that turn above and below the 410-km discontinuity (cusp B' and C'A, respectively) (dotted trace, Figure 3a). In contrast, the model for sector C predicts phase C'A to arrive 1.6 s too early relative to cusp B', were V_S in the transition zone to be high (dash-dotted trace, Figure 3a). Such a sharp boundary in V_S, coinciding with the southern
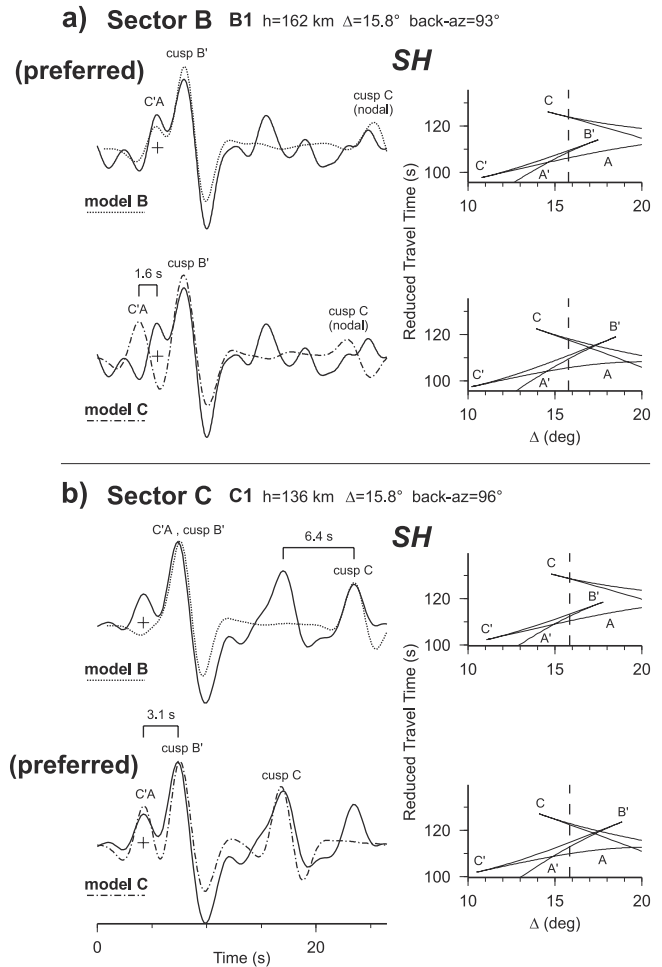

Figure 3. Comparisons between observed (solid traces) and synthetic *SH* waveforms (dotted or dash-dotted traces) observed at NOUC. (a) Result for event B1 on the southern edge of sector B. (b) Result for event C1 on the northern edge of sector C. The two events straddle the southern termination of outboard earthquakes (stars in Figure 1) where there is also an abrupt, lateral change in V_S. In sector C, high V_S in the transition zone is evident from the early arrival of C'A, a ray diving below the 410-km discontinuity, relative to those turning above the discontinuity (cusp B', Figure 3b). The opposite is observed in sector B (Figure 3a). To the right of each waveform is a small portion of the predicted travel time curves (thin solid curves), with a dashed vertical line marking the epicentral distance of the corresponding waveform. Waveforms and travel time curves are labeled according to the convention shown in Figure A1. The layout of deconvolved seismograms places an arrival from the forward branch of a triplication as the peak of an acausal, symmetric wavelet. For comparison, crosses show visually picked first arrivals. In all figures that compare observed and synthetic waveforms, we ignore small misfits in absolute time and shift the synthetic seismograms to highlight comparisons of relative timing between arrivals.
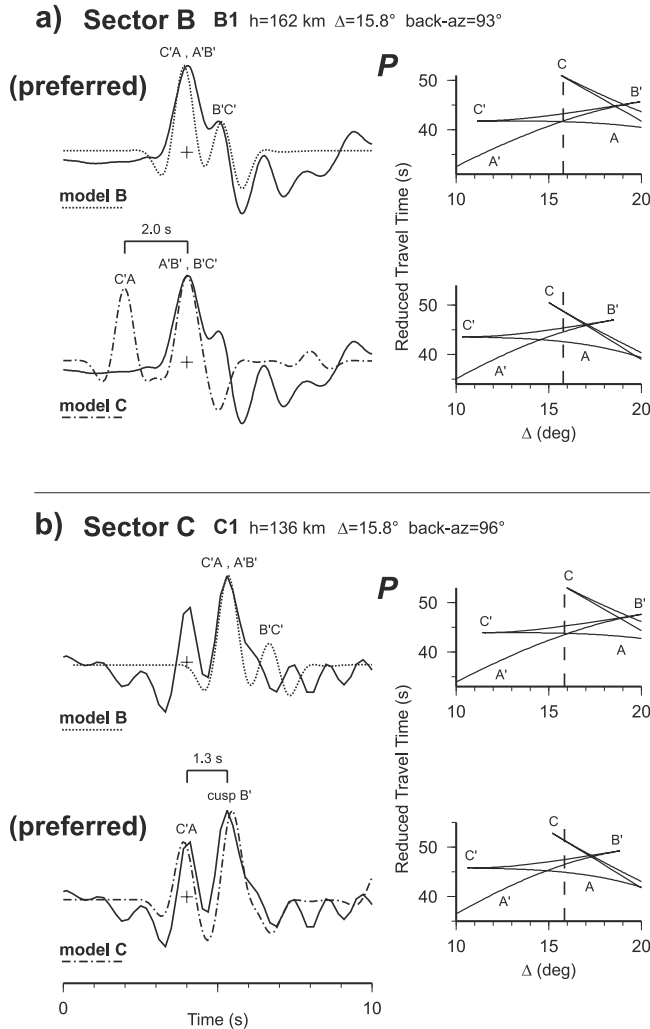
a) Sector B B1 h=162 km Δ=15.8° back-az=93°

b) Sector C C1 h=136 km Δ=15.8° back-az=96°

Figure 4. Comparisons between observed (solid traces) and synthetic P waveforms (dotted or dash-dotted traces) observed at NOUC. Observed waveforms are from the same two events as in Figure 3 showing corresponding results between V_P (Figure 4) and V_S (Figure 3). The layout is the same as that of Figure 3.

termination of outboard earthquakes between sectors B and C, has a corresponding feature in V_P. The latter feature is also robust, backed by clear P waves from events such as B1 and C1 (Figure 4) and others shown in Appendix A of BC2000.

3.2. Source Region of Outboard Earthquakes

[25] By using additional broadband seismograms recorded at station PVC (Figure 1), we have extended the observations of both V_P and V_S to cover the seismogenic zone of nearly all outboard earthquakes (Figure 1). The new observations confirm results for V_P based on measurements at NOUC [BC2000] and show that the entire source region of outboard earthquakes is not associated with high V_P or V_S.

[26] For instance, the P wave train of event A3, sampling the northern edge of outboard earthquakes, shows that phase C′A would arrive 1.8 s too early, if V_P in the transition zone

is as high as that in sector C (Figure 5a). Likewise, the SH wave train of event A6 shows that arrivals comprising cusp C would arrive 2 s too early, were V_S in the transition zone to be high (Figure 5b). In sum, there are now 161 paths crisscrossing the entire source region of outboard earthquakes to conclude that outboard earthquakes in the transition zone are not associated with high V_P and V_S (see additional examples in Figures A3–A5).

[27] This is a very surprising result. The association of deep earthquakes with cold temperature is well established [e.g., *Isacks and Molnar*, 1971; *Molnar et al.*, 1979]. Otherwise, deep earthquakes would not be restricted to zones of recent convergence. Since cold temperature is expected to raise V_P and V_S [e.g., *Creager and Jordan*, 1986; *Grand et al.*, 1997; *Kern*, 1982; *Sinogeikin et al.*, 2001], the absence of high V_P and V_S in the transition zone where earthquakes occur is highly unusual. In the transition zone of the mantle, variations in seismic wave speeds are mainly due to effects of temperature and petrology. Thus, the effect of cold temperature in the source region of outboard earthquakes must be counteracted by a petrologic anomaly.

3.3. Gradients of V_P and V_S

[28] High seismic wave speeds in sectors C and D are accompanied by large apparent gradients of V_P and V_S in the transition zone (Figure 2). A large gradient is constrained by the short time interval between arrivals that turn near the top (C′A) and the bottom of the transition zone (those comprising cusp C). For instance, in the SH waveform of event C1, this interval is at least 6 s shorter than that predicted by the model for neighboring sector B (Figure 3b). In other words, deep-diving rays in sector C travel fast in the deep transition zone where V_S is rapidly increasing with depth.

[29] While a single, linear gradient in the transition zone explains a large number of broadband P and SH wave trains, we observe some clear wave trains that are hard to match without invoking a discontinuity in the middle of the transition zone. This is particularly true for sectors C and D (Appendix B). In fact, the inclusion of such a feature results in synthetic seismograms that can match the first 10–20 s of observed waveforms in fine detail (Figures B1–B2). Thus the apparent large gradient in sectors C and D could result from a midtransition zone discontinuity of 2–3% in V_P and V_S that offsets an otherwise moderate gradient. Since this issue does not affect fundamental differences in average values of V_P and V_S among sectors, we present only the simplest models in Figure 2 with a single, linear gradient in the transition zone. Further discussions of the midtransition zone discontinuity appear in Appendix B.

3.4. Southern Termination of High Seismic Wave Speeds

[30] The region of high V_P and V_S in the transition zone clearly terminates between sectors C and E, as upper bounds of V_P and V_S in sector E do not overlap with lower bounds of corresponding values in sector C (Figure 2). In the transitional sector D, estimates of seismic wave speeds fall in between those of sectors C and E, with some overlap between error bounds for sector D and those for sectors C or E on either side (Figure 2). We conclude that high V_P and V_S in the transition zone of sector C appear to gradually

Sector A

a) *P*   **A3** h=383 km Δ=13.6° back-az=91°

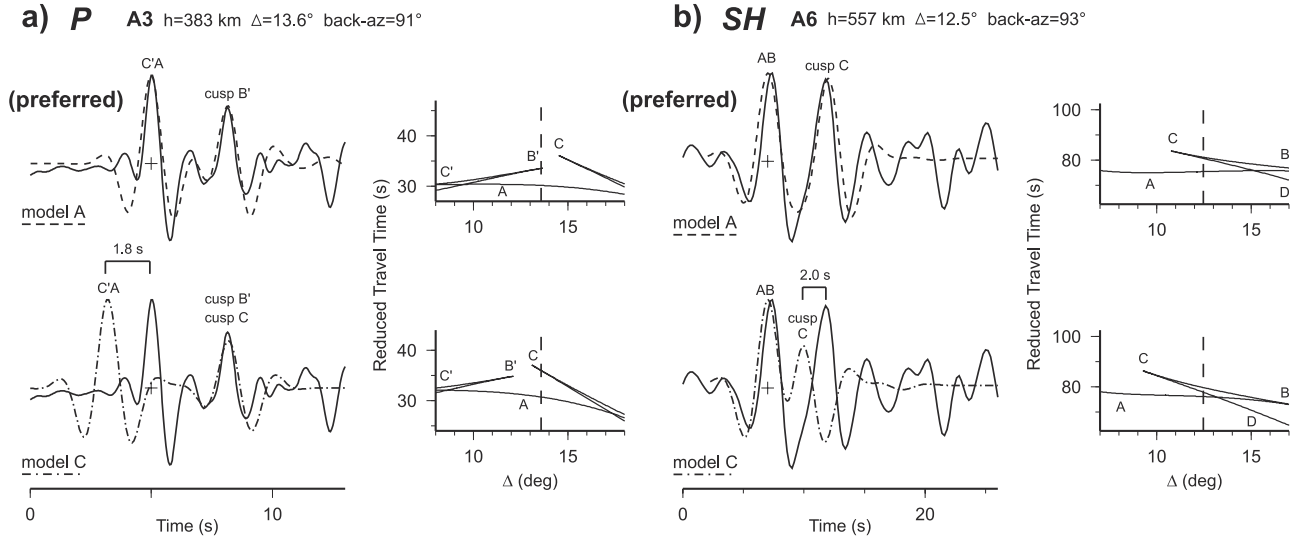**b)** *SH*   **A6** h=557 km Δ=12.5° back-az=93°

Figure 5. Comparisons between observed (solid traces) and synthetic *P* and *SH* waveforms (dashed or dash-dotted traces) observed at PVC, showing results for the northernmost region where outboard earthquakes occur. Short time intervals between arrivals that turn below (C′A) and above (cusp B′) the 410-km discontinuity reflect the lack of high V_P and V_S in the transition zone of sector A. These and similar observations at PVC extend sectors A and B to cover all but a few outboard earthquakes (Figure 1). Layout is similar to that of Figure 3.

terminate southward and do not extend into sector E (Figure 1).

3.5. Lower Mantle

[31] In the uppermost lower mantle, there is some indication that high V_P or V_S exists in sector C and perhaps also in sector B (Figure 2). In contrast to tight constraints available for the transition zone, however, evidence for lateral heterogeneities in the uppermost lower mantle is sparse. The most obvious anomaly is in sector C, where a large contrast in V_S across the 660-km discontinuity is evident from the high amplitude of cusp C (Figure 3b). In this case, V_S is known to be high in the transition zone (Figure 3), so a large contrast across the 660-km discontinuity requires that the uppermost lower mantle also have high V_S. BC2000 made a corresponding case for V_P.

[32] Since the contrast across the 660-km discontinuity is mainly constrained by amplitude information, the current data set results in large uncertainties for estimated values of V_P and V_S in the lower mantle. A related issue is whether high seismic wave speeds also exist in sector B. While there may be some weak indications of such a case for V_P, there are no data available to resolve this issue for V_S (Figure 2). Nonetheless, there is sufficient evidence from many *P* and *SH* waveforms that a prominent fast anomaly cannot exist in the lower mantle beneath sectors A, D, E, and the forearc.

4. Interpretations

[33] The most important result is the lack of high seismic wave speeds in the source zone of outboard earthquakes - an observation first established by lateral variations of V_P [BC2000] and corroborated by similar variations of V_S in this study (Figures 1–2). Such cor-

responding patterns in V_P and V_S provide insights into the nature of deep earthquakes.

[34] In the transition zone of the mantle, seismic wave speeds mainly reflect variations in petrology and temperature. The occurrence of outboard earthquakes alone is sufficient evidence for cold temperature in the source region; otherwise deep earthquakes would not be limited to zones of recent plate convergence [e.g., *Isacks et al.*, 1968; *Wadati*, 1927]. The lack of high seismic wave speeds in sectors A and B is strong evidence for an associated petrologic anomaly that counteracts the effect of cold temperature to raise V_P and V_S. The sharpness of the boundary between sectors B and C, where outboard earthquakes cease to exist and V_P and V_S abruptly rise (Figure 1), is also consistent with petrologic variations, since temperature variations alone would produce a gradual change.

[35] Contenders for the petrologic anomaly must have the potential to trigger deep earthquakes and lower V_P and V_S. Possible candidates include metastable phases such as olivine (α phase) in the cold core of subducted lithosphere, volatiles in the form of hydrous phases, or partial melt induced by volatiles (Figure 6). In general terms, rapid subduction of old, cold lithosphere along the Tonga subduction zone is favorable for transporting and preserving metastable or hydrous phases in the transition zone of the mantle [e.g., *Bose and Navrotsky*, 1998; *Daessler and Yuen*, 1996; *Devaux et al.*, 1997; *Kawamoto et al.*, 1995]. However, two additional conditions (the quantity of material necessary to reduce both V_P and V_S by observed amounts, and the resulting buoyancy of subducted lithosphere) seem to favor metastable α phase.

[36] If hydrous phases can accumulate in the transition zone, embrittlement due to dehydration may be a mechanism for generating deep earthquakes [*Meade and Jeanloz*,

	Metastable Olivine	Hydrous Phases	Partial Melt
Stability in Transition Zone	cold geotherm; favorable in old, fast subducting slab		induced by hydrous phases
Trigger for Deep Earthquakes	transformational faulting	embrittlement due to dehydration	
3% Reduction in V_P	60 % of olivine polymorph in α phase	2.2 wt % H_2O	2 % melt (0.04 wt % H_2O)
Equivalent Reduction in V_S	3 %	2 %	**Reject** 6 % not observed
Slab Density	−1.5 % (only in transition zone)	**Reject** −1 % hinders subduction	~0 %

Figure 6. Candidates for the petrologic anomaly.

1991; *Savage*, 1969; *Silver et al.*, 1995]. The amount of hydrous material, however, is an issue. For instance, hydrous ringwoodite (γ phase), with 2.2% water by weight, has a V_P that is 5.3% lower than that of the anhydrous form [*Inoue et al.*, 1998]. For a reasonable mantle composition of 40–60% olivine, all of olivine polymorphs in sectors A and B must be hydrous to counteract a thermally induced anomaly of +3% in V_P. For a slab to carry such a large amount of hydrous phase, its density would decrease by ~1% [*Inoue et al.*, 1998]. This reduction in density would overwhelm the negative buoyancy of ~0.5% expected for a cold slab [e.g., *Bina*, 1996], making the slab positively buoyant. In such a scenario, subduction could not occur and the slab would never reach the transition zone. To maintain a negatively buoyant slab, the proposed amount of hydrous phases must be halved. Such an amount of hydrous phases, however, would cause merely half of the observed reduction in V_P and V_S. Thus, hydrous phases alone are insufficient to explain our observations (Figure 6).

[37] Alternatively, 0.04 wt % of water freed from hydrous phases could produce 2% of partial melt and cause a 3% reduction in V_P [*Faul et al.*, 1994; *Toomey et al.*, 1998]. Such a small amount of volatiles would not interrupt subduction, as the reduction of density by a minute amount of free water is insignificant and partial melt may not be buoyant in the transition zone [e.g., *Agee and Walker*, 1993]. However, this hypothesis is inconsistent with observed reduction in V_S. The fractional reduction in shear wave speed, $\Delta V_S/V_S$, by a moderate amount of melt (~5%) is expected to be twice as large as that in P wave speed, $\Delta V_P/V_P$ [*Faul et al.*, 1994; *Toomey et al.*, 1998]. Contrary to this scenario, our results show that fractional reductions in both V_S and V_P are comparable in the source zone of outboard earthquakes (Figure 2b).

[38] Meanwhile, metastable olivine remains a viable candidate to account for the disassociation between high V_S and V_P and deep earthquakes. Transformational faulting in metastable olivine has been proposed to trigger deep earthquakes [e.g., *Green and Burnley*, 1989; *Kirby et al.*, 1991]. At the same time, V_P of olivine is ~10–12% less than that of wadsleyite (β phase) and ringwoodite, respectively [e.g., *Katsura and Ito*, 1989; *Sinogeikin et al.*, 1998]. Thus for a mantle composition with 50 ± 10% olivine polymorphs, ~50% of this material must remain in α phase to counteract a thermally induced anomaly of +3% in V_P. This amount of α phase is also expected to produce an equivalent reduction in V_S of 3% [e.g., *Fujisawa*, 1998; *Katsura and Ito*, 1989], consistent with our observations

(Figure 2). Notice that wadsleyite is not a viable alternative for metastable olivine in the lower transition zone where ringwoodite is stable, because the difference in seismic wave speeds between the two phases would be too small to account for observed reductions of 3%.

[39] While metastable olivine alone seems to explain all available observations, one cannot rule out that a combination of the proposed candidates is responsible for the petrologic anomaly. For example, if sufficient metastable olivine is present to account for more than 50% of observed reduction in V_P and V_S, hydrous phases could be responsible for the rest of the anomaly. Nonetheless, low density of water mandates that any presence of hydrous phases must account for less than half of the reduction in seismic wave speeds.

5. Discussion

[40] Taking metastable olivine as the primary source of the petrologic anomaly, the amount of metastable phase proposed here would reduce the overall density of slab below the 410-km discontinuity by ~1.5%, because pure α phase is ~6% less dense than the ambient mantle [*Bina*, 1996; *Okal and Kirby*, 1998]. We emphasize that such a reduction would not make the entire slab buoyant. Instead, one expects a self-limiting process of slab rising and sinking confined to the transition zone.

[41] As a cold slab descends into the transition zone, its tip leaves the stability field of α phase and metastable olivine would make the leading edge of slab buoyant [e.g., *Bina*, 1996; CB2001; *Marton et al.*, 1999]. However, this portion of the slab will never float above the 410-km discontinuity where warmer, less dense olivine of the ambient mantle is also in α phase. This process offers a natural explanation for the subhorizontal configuration of outboard earthquakes (Figure 7). Moreover, a buoyant slab favors retention of subducted material in the transition zone and hinders slab penetration into the lower mantle. This dynamic process provides a simple solution to the puzzling lack of prominent thermal anomaly in the lower mantle beneath Fiji-Tonga where a vast amount of cold slab has been subducting. Sequestering a large amount of subducted material in the transition zone is also a key issue pertaining to the current debate of mantle convection and mixing [e.g., CB2001].

[42] Notice that such a process of sequestering the slab remains viable even if both hydrous phases and metastable olivine are responsible for the petrologic anomaly, because hydrous phases have low density. For instance, in the extreme case where nearly half of the petrologic anomaly is caused by hydrous phase, the slab would be almost neutrally buoyant before entering the transition zone. Once in the transition zone, the amount of metastable olivine required by the observed reduction in V_P and V_S would further reduce the density of the slab by about 0.75%.

[43] At any rate, materials responsible for the petrologic anomaly must be brought down to the transition zone by rapid, recent subduction. Outboard earthquakes are expected to occur in a region where impounding of cold, subducted material is most significant, such that conditions are favorable for the accumulation of metastable olivine or volatiles.

[44] On the basis of detailed analysis of patterns of fault plane solutions, spatial distribution of deep earthquakes, and three-dimensional variations in V_P and V_S (Figures 1–2),
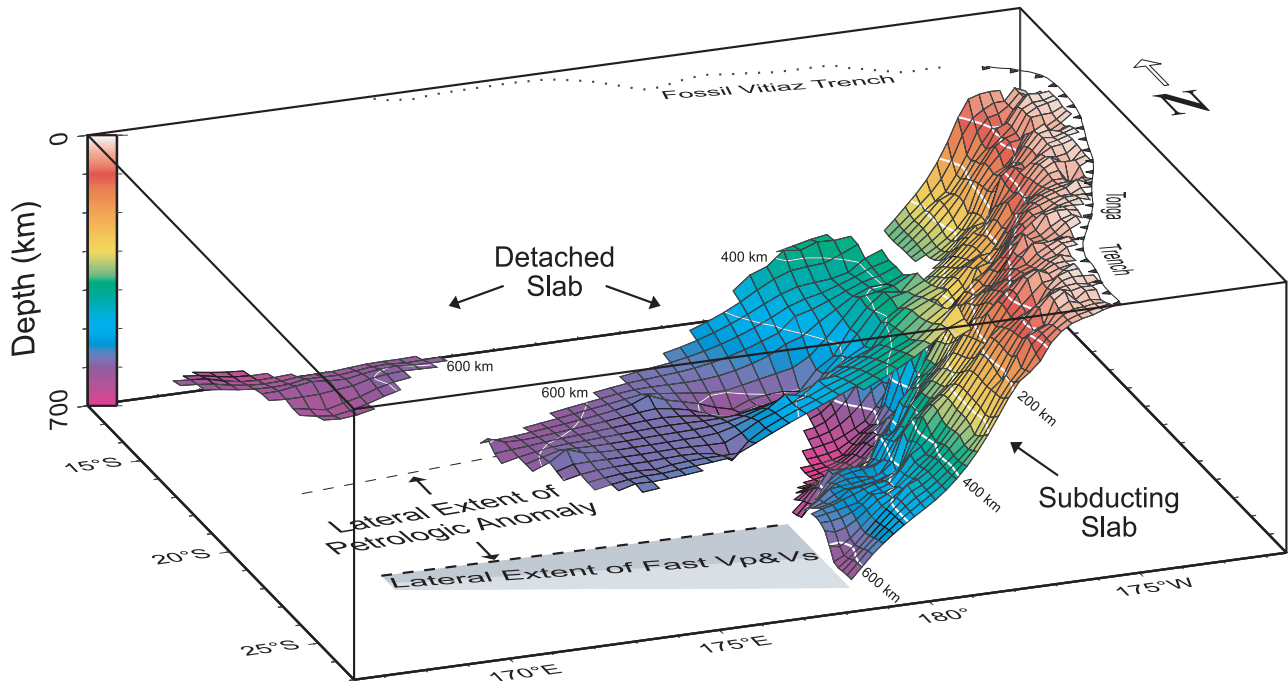
Figure 7. A three-dimensional rendition of seismicity beneath the Tonga back arc (with no vertical exaggeration). For the region south of 15°S, two separate surfaces, representing a detached remnant of slab and the actively subducting lithosphere, are constructed from hypocenters of outboard earthquakes and those in the WBZ, respectively [CB2001]. An additional surface indicates the isolated cluster of earthquakes northeast of the Vanuatu trench. Contour lines are drawn at intervals of 100 km in depth. The juxtaposition of slab retains a large amount of subducted material above the lower mantle.

CB2001 identified the outboard earthquakes discussed here as part of a large-scale remnant of subducted lithosphere. The entire subhorizontal remnant covers an area up to 1500 km by 1000 km and is detached from actively subducting lithosphere (Figure 7). The juxtaposition of a large-scale, detached remnant of slab and a steep-dipping, active Wadati-Benioff zone (WBZ) provides a specific process of how buoyant, subducted material is being sequestered in the transition zone. Such a process, in turn, explains why a prominent remnant of slab is missing in the lower mantle beneath Tonga.

[45] In this scenario, outboard earthquakes delineate only the coldest core of detached slab where metastable olivine or volatiles is preserved. Large thermal inertia of subducted lithosphere would imply that a diffuse aureole of cold temperature must surround the coldest core marked by outboard earthquakes. This offers a natural explanation for high seismic wave speeds in sector C and apparently gradual, southward termination of such an anomaly in sector D (Figures 1–2).

[46] The magnitude of anomaly caused by cold temperature depends on how V_P and V_S change with temperature, a poorly determined relationship for realistic petrology under conditions appropriate for the transition zone. In samples of olivine polymorphs and peridotite, estimates of temperature coefficients (dV/dT) are approximately −0.4 to −0.5 m s^{-1} °C^{-1} and −0.3 to −0.4 m s^{-1} °C^{-1} for V_P and V_S, respectively [Kern, 1982; Li et al., 1998; Sinogeikin et al., 2001]. Thus an increase of 3% in V_S implies a temperature anomaly of 400–550°C in sector C. Such an anomaly (averaged over the thickness of the slab) is even below predictions of 500 to 700°C from thermomechanical

models of the Tonga WBZ [e.g., Insergueix et al., 1997; Stein and Stein, 1996]. Corresponding estimates from V_P are somewhat larger, about 600–800°C. Given the exceedingly fast rate of subduction (∼200 mm yr^{-1}) and old age of Pacific plate being subducted (>100 Ma), such estimates still by and large overlap with the realm of theoretical predictions. Furthermore, the southward, seemingly gradual decrease of the anomaly from sectors C to E is consistent with a thermal anomaly that is strong in sectors A and B to retain metastable olivine, diminishes in sectors C and D where metastable olivine is no longer viable, and finally becomes indistinguishable from the ambient transition zone in sector E.

[47] Detailed history of a slab, once subducted, is very difficult to unravel since it leaves little trace in the geologic record at the surface. In Tonga, further complication comes from possible high V_P and V_S in the lower mantle, suggesting that some slab material, either associated with the actively subducting WBZ or remnant slab, may have penetrated the 660-km discontinuity [BC2000; van der Hilst, 1995; Zhou, 1996]. Following the work of previous researchers [Barazangi et al., 1973; Billington, 1980; Fischer et al., 1991; Hamburger and Isacks, 1987; Okal and Kirby, 1998], CB2001 proposed that relic subduction of the Pacific plate along the Vitiaz trench would be a natural source for the detached lithosphere. Green [2001] suggested an alternative hypothesis that the slab remnant is from the tip of eastward subducting slab that broke off from the active WBZ due to the buoyancy of metastable olivine. In this case, a diffuse aureole of cold temperature accompanied by fast V_P and V_S must also exist to the north of outboard
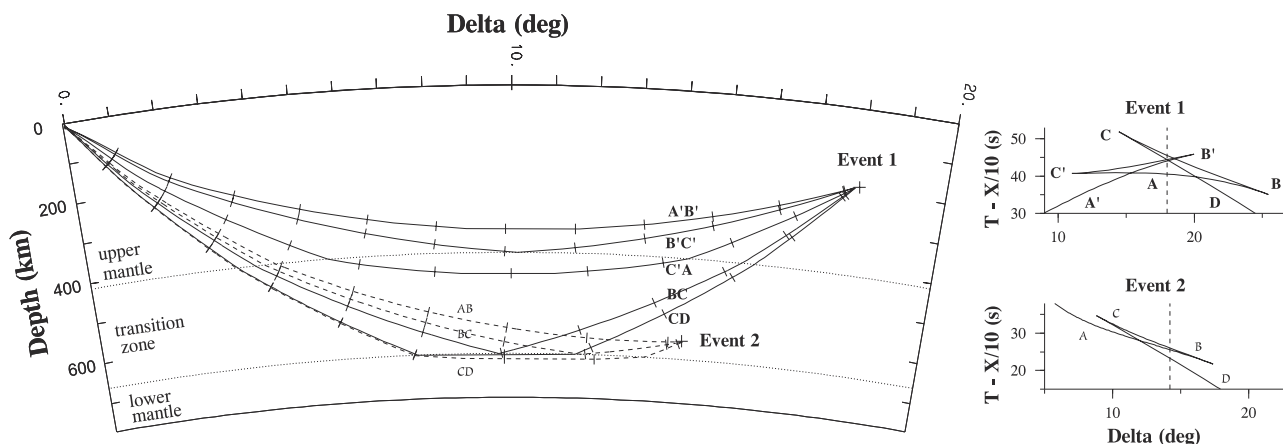
Figure A1. (left) Schematic cross section illustrating ray paths for two earthquake sources at different depths. A source located above the 410-km discontinuity produces two sets of triplicate arrivals (solid curves, event 1), whereas a source below the 410-km discontinuity produces only one set of triplicate arrivals (dashed curves, event 2). Short bars along each ray path mark intervals of 20 s in travel time. (right) Reduced travel time curves. Dashed vertical lines mark epicentral distances for each event.

earthquakes, mirroring sectors C and D, a prediction that cannot be tested with the present coverage of seismic stations. At any rate, the clear disassociation between outboard seismicity and high values of V_P and V_S in the transition zone of the mantle provides strong evidence for a direct link between deep earthquakes and mantle petrology.

[48] Finally, we briefly discuss the issue of whether the extent of petrologic anomaly can contain the source volume of the largest mantle earthquakes. This is not an issue per se for outboard earthquakes that reach up to M_w 7.1 near Tonga [CB2001]; however, the largest deep earthquakes that reach over M_w 8 almost always occur near the tip of active Wadati-Benioff zones. There are a large number of studies on the latter subject in the past decade (see, for instance, a review by *Green and Houston* [1995, and references therein]). One specific issue is whether the largest earthquakes can occur within a narrow wedge of metastable olivine. Recently *Wu and Chen* [2001] summarized results from seven of the largest deep earthquakes and in some cases the extent of rupture seems unusually large. Nevertheless the issue remains open for debate because several possible explanations are available to explain these cases [e.g., *Karato et al.*, 2001; *Kirby et al.*, 1995, 1996; *McGuire et al.*, 1997].

6. Conclusions

[49] Using a sequence of seismic profiles constructed from broadband waveforms and travel times, we constrain three-dimensional variations of V_P and V_S beneath the Fiji-Tonga region where subduction is taking place at a staggering rate of 200 mm yr^{-1}. We find that the overall distribution of V_P and V_S are similar (Figure 2). Prominent anomalies of high V_P and V_S occur in the transition zone of the mantle. The anomalies terminate sharply where outboard earthquakes occur and V_P and V_S abruptly drop by about 3% to values close to those beneath the forearc. Spatial coverage of our data is now sufficiently dense to show that the entire seismogenic zone of outboard earthquakes is not associated with high V_P and V_S (Figure 1). It follows that compositional or mineralogical effects to lower

V_P and V_S must have counteracted the opposing effect of cold temperature, as implied by the presence of deep earthquakes. We interpret that the outboard earthquakes occur in a region where impounding of cold, subducted material is most significant, a condition favorable for the accumulation of metastable olivine or volatiles. Such materials are obvious candidates for lowering V_P and V_S, and for triggering deep earthquakes. However, the quantity of hydrous phases required to reduced V_P and V_S by the observed amount is likely to make the entire slab too buoyant to subduct. Moreover, the observed reduction in V_S is small enough to practically eliminate partial melt (induced by dehydration) as a potential candidate. At the moment, metastable olivine seems to be viable to account for the absence of high V_P and V_S in the source zone of deep earthquakes. In a cold slab subducting at a high rate, metastable olivine should be most abundant and would make the slab buoyant at depths below the 410-km discontinuity. Such a scenario explains why leading portions of fast subducting material may successively stagnate in the transition zone.

Appendix A: Modeling of Waveforms

[50] The standard sampling rate of 20 samples s^{-1} initiated at different times at the three stations used in this study: in 1993 at NOUC, 1995 at PVC, and 1992 at RAR. Prior to these times, the rate is 5 samples s^{-1} at NOUC and PVC during 1989–1992 and 1994–1995, respectively. Nevertheless, in each case, the instrument response has always been truly broadband, so seismograms with different sampling rates can be directly compared with an obvious limitation that the resolution in time is ±0.2 s for some data prior to 1995. The lower sampling rate also causes some seismograms to appear not as smooth traces when plotted (e.g., event C1 in Figure 4). During the deconvolution to remove source effects, we apply bandpass filters with corner frequencies of ∼0.2 to ∼2.0 Hz and ∼0.1 to ∼0.5 Hz for P and S waves, respectively. In both cases, the passband is below the Nyquist frequency of all
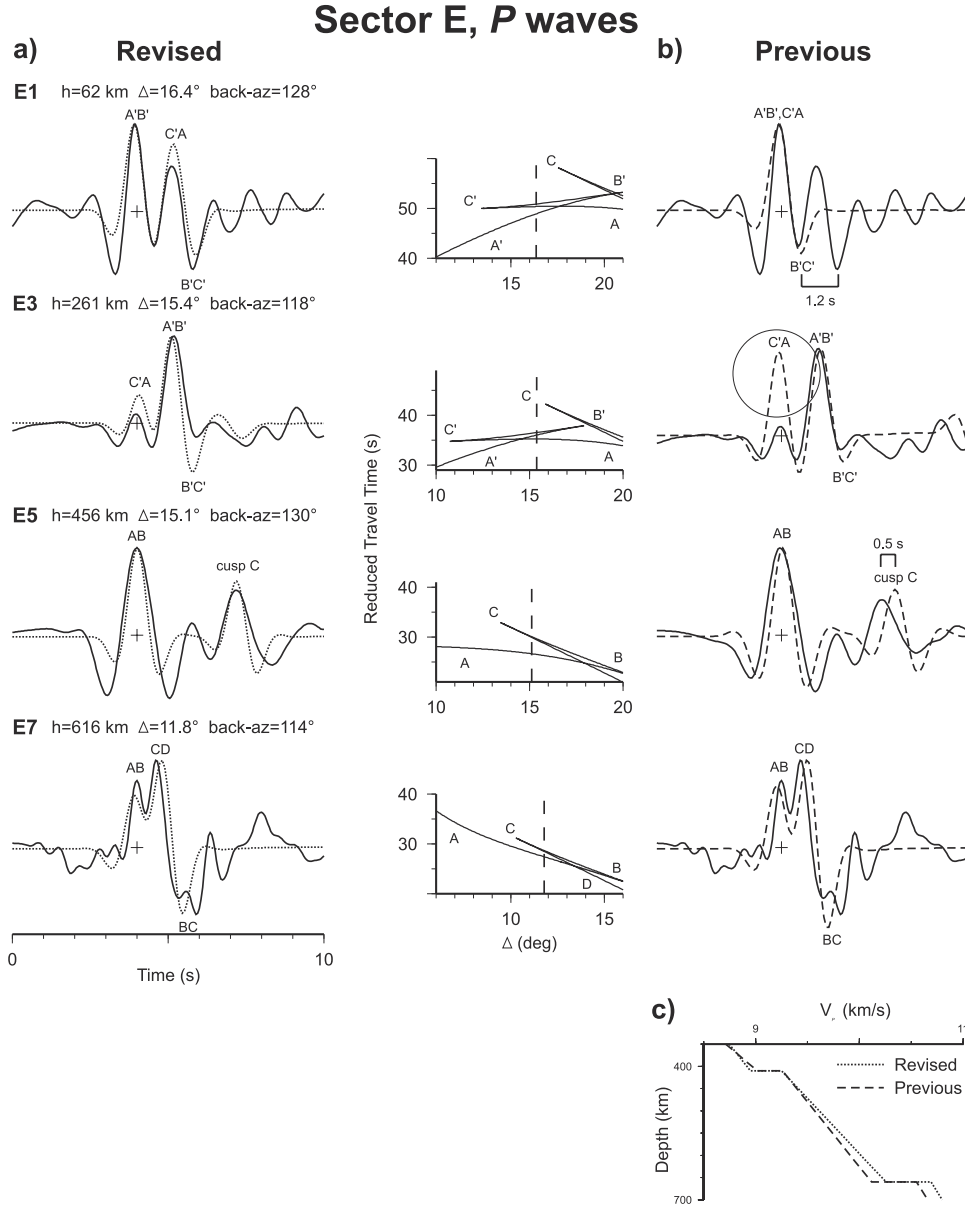
Figure A2. Revised results for sector E, utilizing new *P* waveforms observed at NOUC (solid traces). Layout is similar to that of Figure 3. (a) Comparison of observed waveforms with synthetic seismograms (dotted traces) from the revised model. (b) Comparison of observed waveforms with synthetic seismograms (dashed traces) from a previous model [BC2000]. (c) Revised and previous models of V_P as a function of depth. The two models differ only slightly.

data, and in general, the predominant wavelength of wavelets used in this study is ∼10 km for *P* waves and ∼20 km for *S* waves.

[51] From this data set, we construct profiles with a range of epicentral distances and focal depths (e.g., Figure A1). We first seek the simplest model that explains all waveforms and travel times within a narrow sector of back azimuths. Then we expand the range of back azimuths to include neighboring paths until the model can no longer account for all observed waveforms and travel times. This process defines the boundaries of each sector.

[52] In each sector, for regions above the transition zone, we use absolute timing of wide-angle reflections off the 410-km discontinuity to constrain the root-mean-square (RMS) V_P and V_S. Within the transition zone, relative timing between reflections off the 410- and 660-km discontinuities constrains the average V_P and V_S, while relative timing between rays that turn at different depths constrains the gradient in V_P and V_S. Relative timing and amplitudes between arrivals turning just above and below a discontinuity constrain both the increase in V_P and V_S and depth of that discontinuity; the latter is taken as common to both V_P and V_S. Each free parameter is also subject to a priori constraints, limited by extreme values summarized by *Kennett* [1993]. We assume that gradients of V_P and V_S below the 660-km discontinuity are the same as those of the

A1 h=135 km Δ=17.4° back-az=85°

Sector A, *P* waves

A3 h=383 km Δ=13.6° back-az=91°

A7 h=563 km Δ=13.1° back-az=95°

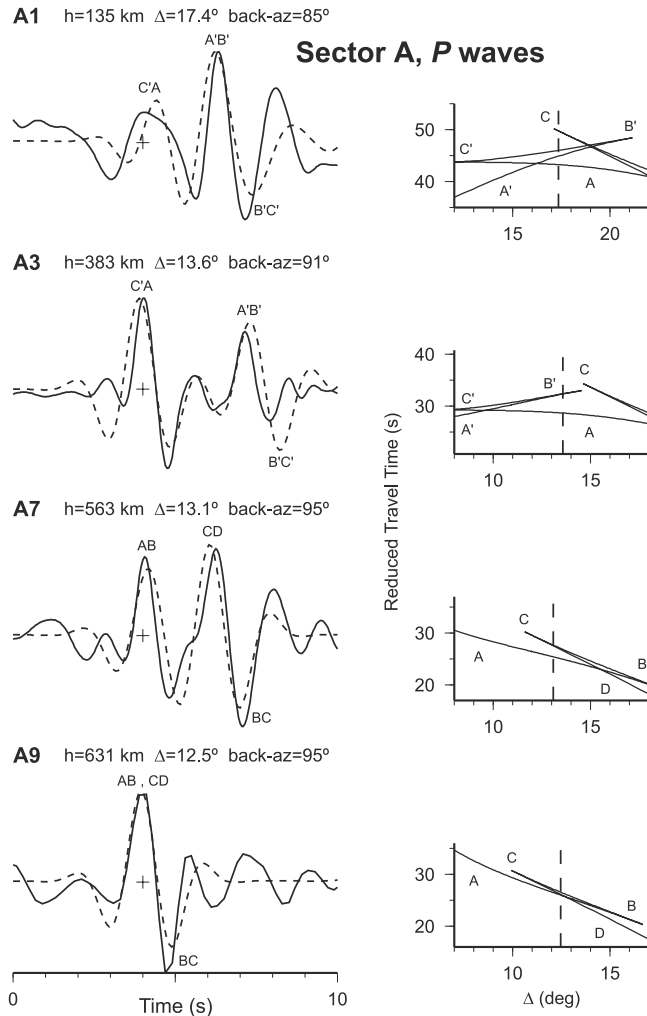
A9 h=631 km Δ=12.5° back-az=95°

Figure A3. Comparisons between *P* waveforms observed at PVC (solid traces) and synthetic seismograms (dashed traces) from the best fitting model for sector A. These data sample the northernmost region where outboard earthquakes occur. Layout is similar to that of Figure 3.

iasp91 model [*Kennett and Engdahl*, 1991], because in our data set, rays sampling the lower mantle turn at similar depths just below the 660-km discontinuity, providing little constraint on the gradients.

[53] We search the model space through forward modeling to determine best fitting models for each sector. The best fitting model minimizes misfits between observed and synthetic seismograms in relative timing, relative amplitudes, and absolute timing. Specific examples of how V_P and V_S are determined are discussed in section 3 (Figures 3–5).

A1.   Key Waveforms and Summary of Best Fitting Models

[54] In addition to the waveforms shown in Figures 3–5, we present a select set of waveforms that are particularly important for constraining V_P and V_S in this study. To complement the set of *P* waveforms in BC2000, we begin with new *P* waveforms at the southern and northern edges of our study region (Figures A2 and A3, respectively), and then show *SH* waveforms for each sector in alphabetical

order for easy reference (Figures A4–A9). For each best fitting model, specific values of parameters are shown in Tables A1–A2.

[55] In general, the new data set sharpens the demarcation between sectors C and B to less than 30 km (Figure 1), where a drop in V_P and V_S coincides with the onset of outboard earthquakes (Figures 3–4). Considering the sharpness of such lateral variations, it is perhaps not surprising that features delineated in this study cannot be resolved by previous studies using travel time tomography with cell sizes of 200–400 km. In fact, such studies showed inconsistent results, even though identical data sources and similar techniques were used [cf. *van der Hilst*, 1995; *Zhou*, 1996]. In contrast, we have designed our experiment specifically to target the region of interest.

[56] Many other new waveforms collected in this study, particularly those recorded at PVC, now expand the northern limit of sector A to include all but a few outboard earthquakes (Figure 1). The improved coverage in sectors A and B corroborates the result for *P* waves by BC2000 (Figure A3). More important, new results from *S* waves
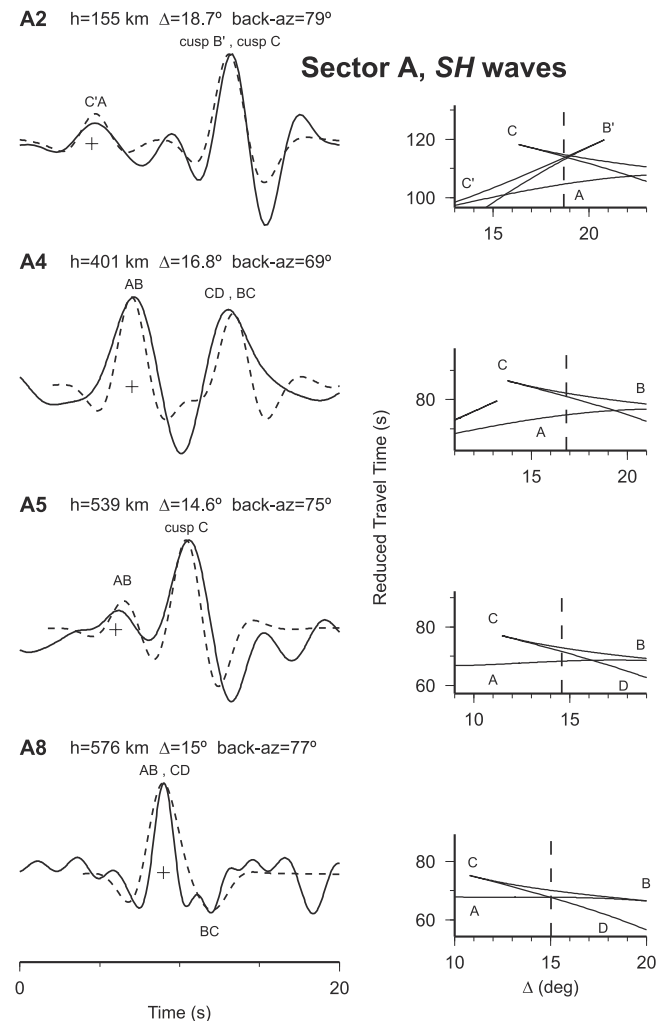
A2 h=155 km Δ=18.7° back-az=79°

cusp B' , cusp C

Sector A, *SH* waves

A4 h=401 km Δ=16.8° back-az=69°

A5 h=539 km Δ=14.6° back-az=75°

cusp C

A8 h=576 km Δ=15° back-az=77°

Figure A4. Comparisons between *SH* seismograms observed at NOUC (solid traces) and synthetic seismograms (dashed traces) predicted from the best fitting model for sector A, the northern half of the region where outboard earthquakes occur. Layout is the same as that of Figure A3.
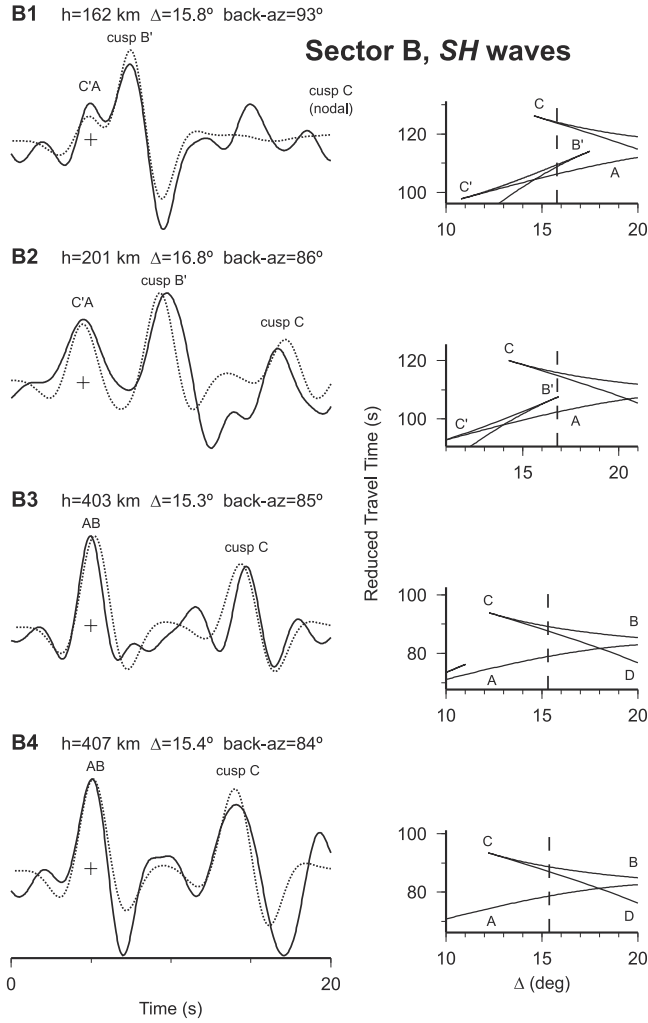
Figure A5. Comparisons between *SH* seismograms observed at NOUC (solid traces) and synthetic seismograms (dotted traces) predicted from the best fitting model for sector B, the southern half of the region where outboard earthquakes occur. Layout is the same as that of Figure A3.

show corresponding patterns between V_P and V_S in all sectors (Figures A4–A9 and Figure 2).

[57] For V_P, using refined locations of epicenters [*Engdahl et al.*, 1998] and an expanded set of waveforms, current results are similar to our previous report [BC2000]. The only revision to V_P that warrants further discussion is the addition of five new *P* waveforms in sector E, where the previous model was based on a limited set of eight waveforms in BC2000. The set of waveforms now includes rays turning above the 410-km discontinuity as the unobstructed, first arrival (A′B′ in event E1, Figure A2). When combined with cases where rays turning below the 410-km discontinuity become the first arrival (C′A in event E3, Figure A2), the contrast in V_P across the 410-km discontinuity is constrained to be about 3.3% (Table A1), slightly larger than the previous estimate (Figure A2c). Similarly, deep-diving rays turning near the 660-km discontinuity improve our ability to resolve the gradient of V_P in the transition zone (events E5 and E7, Figure A2a and A2c). None of these revisions affect the original point that sector E marks the

southern termination of high V_P in the transition zone [BC2000].

A2. Error Analysis

[58] To estimate error bounds, we explore the model space by perturbing the best fitting models until synthetic seismograms show large misfits in relative timing, relative amplitudes, or absolute timing. Figure 2 summarizes the best fitting models and bounds on acceptable values of V_P and V_S. For the best fitting model of any single sector, the mean misfit in relative timing between any two arrivals is close to zero (<0.1 s), with a standard deviation of approximately ±0.2 to ±0.4 s for V_P and V_S, respectively.

[59] In a given sector, we reject models if any predicted relative time is larger than two standard deviations of the prediction from the best fitting model. In practice, the ranges of cutoff values are 0.35–0.55 s for *P* and 0.7–1.1 s for *SH*, consistent with V_P/V_S of ~1.8. In each case, the criterion corresponds roughly to one quarter of the average period of observed pulses.
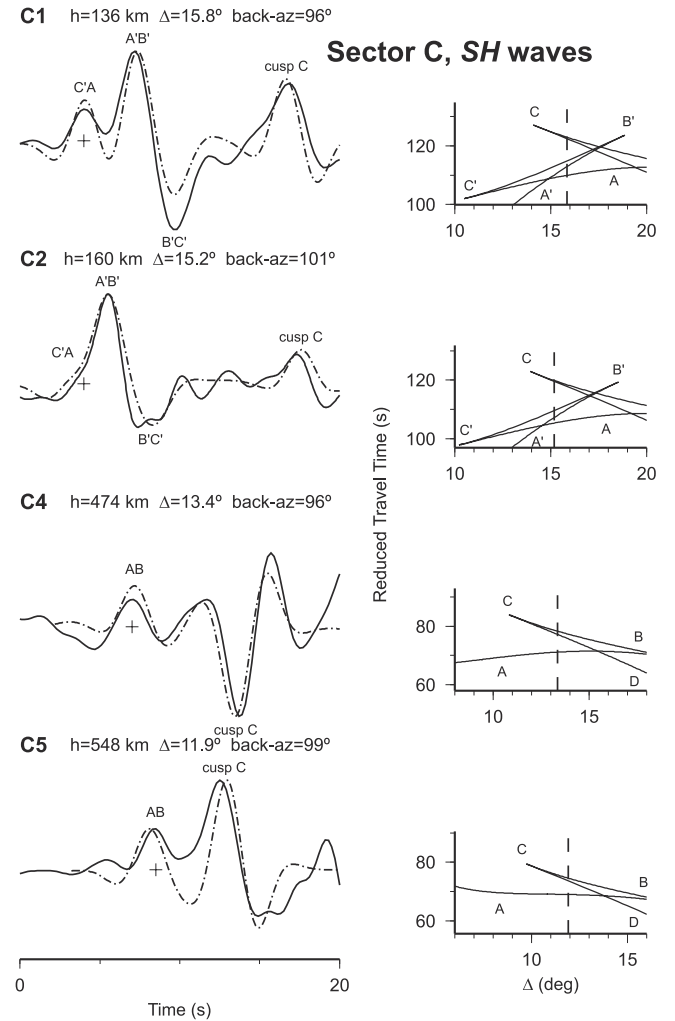

Figure A6. Comparisons between *SH* seismograms observed at NOUC (solid traces) and synthetic seismograms (dash-dotted traces) predicted from the best fitting model for sector C, just south of the outboard earthquakes. Layout is the same as that of Figure A3.
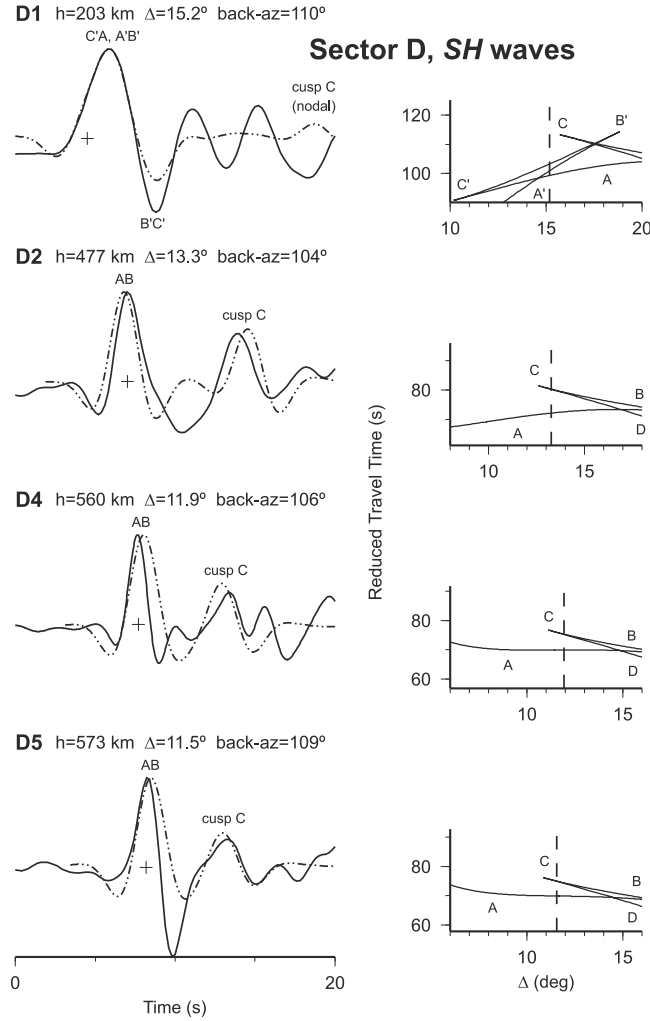
Figure A7. Comparisons between *SH* seismograms observed at NOUC (solid traces) and synthetic seismograms (dash-dotted traces) predicted from the best fitting model for sector D. Layout is the same as that of Figure A3.

Figure A8. Comparisons between *SH* seismograms observed at NOUC (solid traces) and synthetic seismograms (dotted traces) predicted from the best fitting model for sector E, the southernmost portion of the back arc sampled by this study. Layout is the same as that of Figure A3.

[60] Since earthquakes occur in vastly different sizes, we normalize all peak amplitudes to unit scale, preserving only relative amplitudes. Our best fitting models produce a mean misfit of about 0 ± 30% in relative amplitudes, a standard deviation comparable to the minimum signal-to-noise ratio of the data (3:1). We reject a model if the predicted amplitude ratio between any two arrivals is off by more than a factor of two.

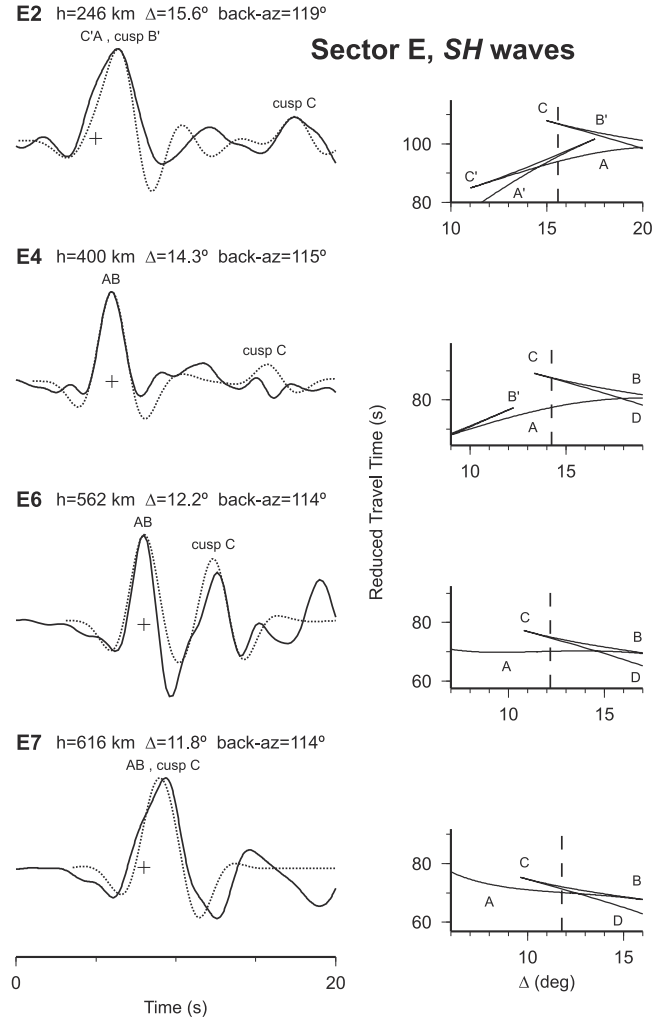[61] The misfits in relative timing and amplitude are likely due to either random errors in epicenter location or slight variations in V_P and V_S within a sector. For instance, in a worst-case scenario, a mislocation of ±10 km in epicenter could affect relative timing and relative amplitude in *P* waveforms by approximately ±0.3 s and ±30%, respectively. Either way, variations in V_P and V_S between sectors are beyond conceivable variations within sectors (Figure 2), so relative timing and amplitudes are sufficient to distinguish different sectors. Absolute timing is not required for this purpose.

Table A1. Summary of Best Fitting Models for V_P

| Sector	RMS Value Above 410 km, Difference From Forearc,%	Contrast Across 410-km Discontinuity, %	Gradient in Transition Zone, 10^{-3} km s^{-1} km^{-1}	Contrast Across 660-km Discontinuity, %
A	−2.4 ± 0.5	5.9 (+0.2/−0.7)	3.75 (+0.37/−0.10)	4.3 (+0.7/−0.4)
B	−2.6 ± 0.6	5.1 (+0.5/−0.3)	3.55 (+0.10/−0.12)	8.0 (+0.4/−1.1)
C	−3.8 ± 0.6	5.9 (+0.3/−0.1)	5.20 (+0.25/−0.55)	5.2 (+0.2/−0.2)
D	−3.1 ± 0.6	5.2 (+1.1/−0.4)	4.82 (+0.23/−0.62)	2.9 (+0.2/−0.5)
E	−2.2 ± 0.6	3.3 (+0.5/−0.2)	4.03 (+0.67/−0.65)	4.1 (+0.7/−1.4)
Forearc	-	4.5 (+0.2/−0.1)	4.20 (+0.25/−0.20)	4.2 (+0.9/−0.3)
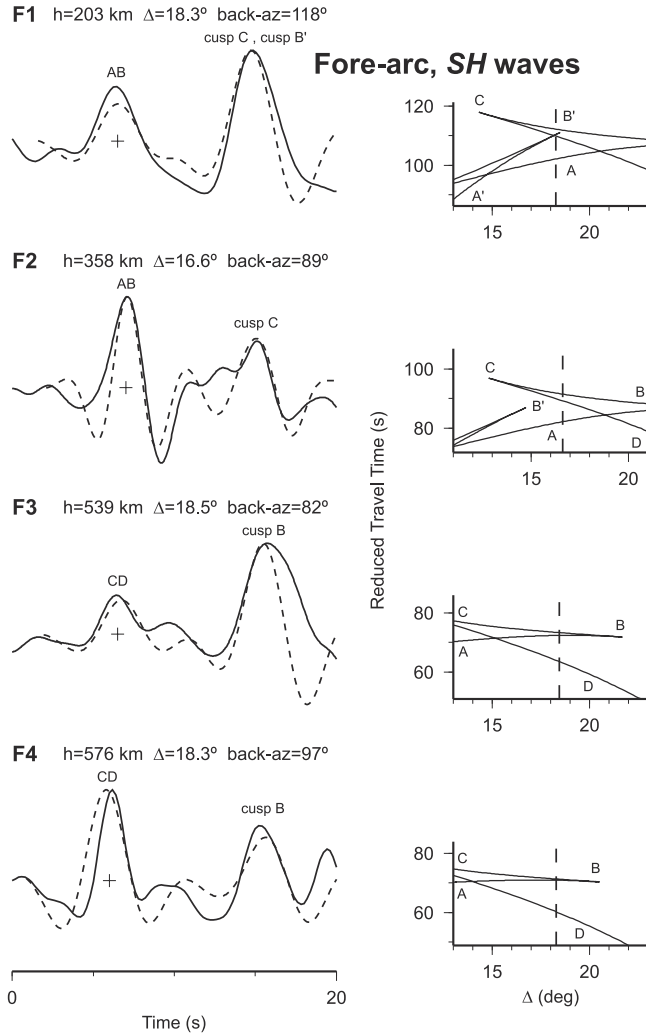
Figure A9. Comparisons between *SH* seismograms observed at RAR (solid traces) and synthetic seismograms (dashed traces) predicted from the best fitting model for the forearc. Layout is the same as that of Figure A3.

[62] In any single sector, the mean misfit in absolute timing of first arrivals is close to zero (<0.1 s). The ranges of standard deviations among sectors are $1.0-1.3$ s for *P* and $1.1-1.6$ s for *S*. This pattern in absolute timing resembles random errors due to mislocation of epicenters by approximately ± 10 km. Since one can never rule out possible errors in location and origin time of any earthquake, we consider two extreme cases. In the first case, we attribute fluctuations in absolute timing to mislocation alone, not contributing to uncertainties in V_P and V_S. The result is a minimal estimate of errors in V_P and V_S. In the second case, we assume fluctuations in absolute timing solely reflect variations in V_P and V_S, resulting in a maximal estimate of errors in our models. The actual bounds on V_P and V_S probably lie between these two extreme cases. The final error bounds we report use the maximal estimate of errors, including the trade-off between depths to seismic discontinuities and average values of V_P and V_S (Figure 2). Additional considerations on modeling and error analysis, including some heuristic examples, are presented in BC2000.

[63] It is important to bear in mind that changes in absolute timing affect primarily the numerical values of average V_P and V_S, not the gradient of V_P and V_S over depth or the increases in V_P and V_S across discontinuities. Thus acceptable models in the maximum estimate of errors must still preserve the shape of how V_P and V_S changes over depth. For instance, the lowest possible V_P and V_S in the transition zone and the highest possible V_P and V_S in the lower mantle as depicted in Figure 2 are not an acceptable combination, because the increase in V_P and V_S across the 660-km discontinuity would be too large.

Appendix B: Midtransition Zone Discontinuity

[64] The existence of a midtransition zone discontinuity is controversial [e.g., *Benz and Vidale*, 1993; *Bock*, 1994; *Deuss and Woodhouse*, 2001]. First, such a discontinuity does not appear to be a global feature [e.g., *Gossler and Kind*, 1996; *Gu et al.*, 1998]. Second, when observable, the depth of the so-called "520-km" discontinuity varies considerably from 500 to 570 km [e.g., *Deuss and Woodhouse*, 2001; *Flanagan and Shearer*, 1998]. Third, the reported size of discontinuity in V_P and V_S varies widely in different regions of the globe, from as small as 0.1% to as large as 5% [e.g., *Kato and Jordan*, 1999; *Shearer*, 1991]. Following the work of BC2000 on *P* waves that suggested the presence of such a discontinuity beneath the Tonga back arc, we investigate this issue with an expanded set of *P* and *SH* waveforms (Figures B1–B2).

[65] In sectors C and D, where average values of V_P and V_S are high in the transition zone, we observe strong arrivals in *P* and *SH* waveforms that are difficult to explain without invoking a discontinuity in the middle of the transition zone. For example, in sector C, a clear, strong phase (C'') arrives between the first arrival (AB) and the arrival of cusp C (Figures B1a and B2a). If V_P and V_S vary smoothly in the transition zone, no arrival is expected between AB and cusp C (left column, Figures B1a and B2a). In contrast, models with an additional discontinuity in V_P and V_S produce a caustic arrival such that all prominent features in the first $10-20$ s of observed *P* and *SH* waveforms are matched in detail (right column, Figures B1a and B2a).

[66] The contrast across the discontinuity ($\sim 2-3\%$ in both V_P and V_S) is comparable to a number of reports elsewhere [e.g., *Ryberg et al.*, 1997]. Such values would replace a single, high gradient by two layers of moderate gradients. For example, in sector C the gradient in V_P is reduced from 5.20×10^{-3} km s^{-1} km^{-1} to 3.70×10^{-3} km s^{-1} km^{-1}. The corresponding reduction for V_S is from 2.55×10^{-3} km s^{-1} km^{-1} to 1.80×10^{-3} km s^{-1} km^{-1} (Figure B3a).

[67] Timing and amplitude of cusp C'' arrivals also constrain the depth and sharpness of the midtransition zone discontinuity. If the increase in V_P and V_S is perfectly sharp (as assumed in generating the synthetic seismograms in Figures B1–B2), then the depth of the discontinuity is constrained to be 570 ± 20 km in sector C and 585 ± 15 km in sector D. Equivalently, if the contrast in V_P and V_S spreads over a range of depths with a linear gradient, the thickness of such a broad discontinuity is approximately $30-40$ km (Figure B3). These estimates take into account the trade-off between depth of the discontinuity and

Table A2. Summary of Best Fitting Models for V_S

Sector	RMS Value Above 410 km, Difference From Forearc,%	Contrast across 410-km Discontinuity, %	Gradient in Transition Zone, 10^{-3} km s^{-1} km^{-1}	Contrast Across 660-km Discontinuity, %
A	0.0 ± 0.4	7.1 (+0.3/−0.1)	1.50 (+0.20/−0.07)	6.2 (+0.4/−0.5)
B	-1.9 ± 0.3	4.6 (+0.9/−0.4)	1.57 (+0.05/−0.13)	8.9 (insufficient data)
C	-2.0 ± 0.3	6.4 (+0.9/−0.7)	2.55 (+0.05/−0.16)	7.9 (+2.3/−1.5)
D	-1.4 ± 0.4	5.9 (+2.0/−0.1)	2.32 (+0.13/−0.22)	4.8 (+0.8/−0.5)
E	-0.6 ± 0.4	3.2 (+0.1/−0.1)	2.50 (+0.05/−0.21)	5.2 (+1.6/−0.6)
Forearc	-	5.9 (+0.9/−0.8)	1.56 (+0.09/−0.06)	8.9 (+0.4/−0.5)

average values of V_P and V_S above the discontinuity [BC2000].

[68] A clear arrival associated with cusp C″, unobstructed by interference from other seismic phases, can appear only over a narrow range of epicentral distances and focal depths. In our data set, eight events in sectors C and D meet this restrictive condition, resulting in an unequivocal C″ arrival in eight P and four SH waveforms. Of the remaining waveforms, 22 render indirect evidence for a midtransition zone discontinuity: Small intervals of relative timing between arrivals sampling different depths clearly reflect a rapid increase in V_P and V_S with depth (e.g., Figures 3b and A6−A7).

[69] Outside of sectors C and D, our data indicate that the midtransition zone discontinuity must have a contrast of 1% or less in V_P and V_S. The detectable contrast of such a small discontinuity depends on epicentral distances/focal depths and fault plane solutions, which affect the relative timing and amplitude of arrivals, respectively. Assuming a reasonable range of depths between 500 and 580 km for the discontinuity, in sector E and the forearc, the predicted amplitude of the C″ caustic becomes appreciably larger than that observed if the contrast is over 1% (Figures B1c and B2c). In sectors A and B, the corresponding threshold is also about 1%, with three waveforms suggesting a small contrast close to 0.6%.

[70] Phase transitions such as the transformation from wadsleyite (β phase) to-ringwoodite (γ phase) and that from garnet to Ca-perovskite have been proposed to explain a midtransition zone discontinuity [e.g., *Ita and Stixrude*, 1992; *Katsura and Ito*, 1989; *Koito et al.*, 2000]. The increase in V_P and V_S predicted from the transition of β to
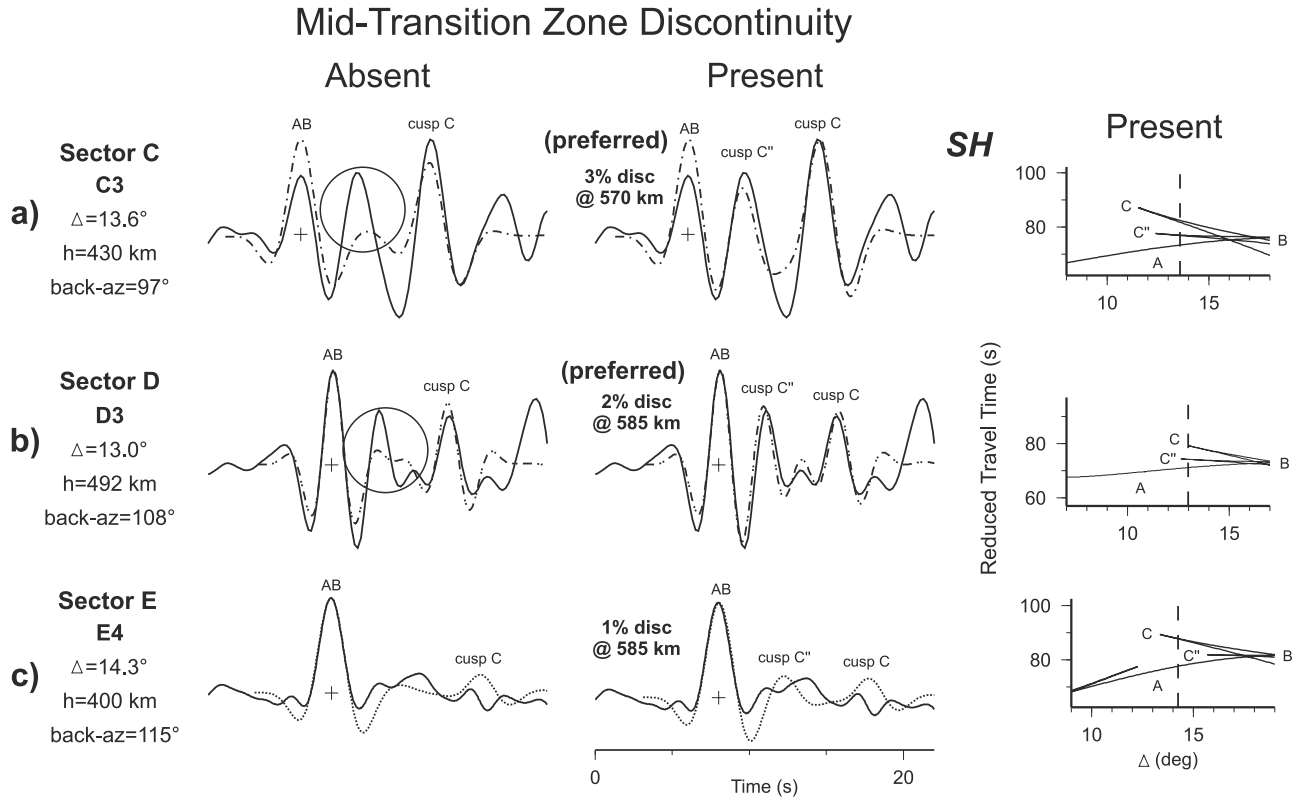

Figure B1. Comparisons between observed (solid traces) and synthetic SH waveforms (dash traces), showing evidence for or against a sizable midtransition zone discontinuity. Layout is similar to that of Figure 3. In sectors C and D where average V_S is high, a clear, caustic arrival (C″) cannot be matched unless a discontinuity of 2−3% exists in the lower portion of the transition zone (Figures B1a and B1b). In sector E (Figure B1c), the data allows a discontinuity of 1% or less.
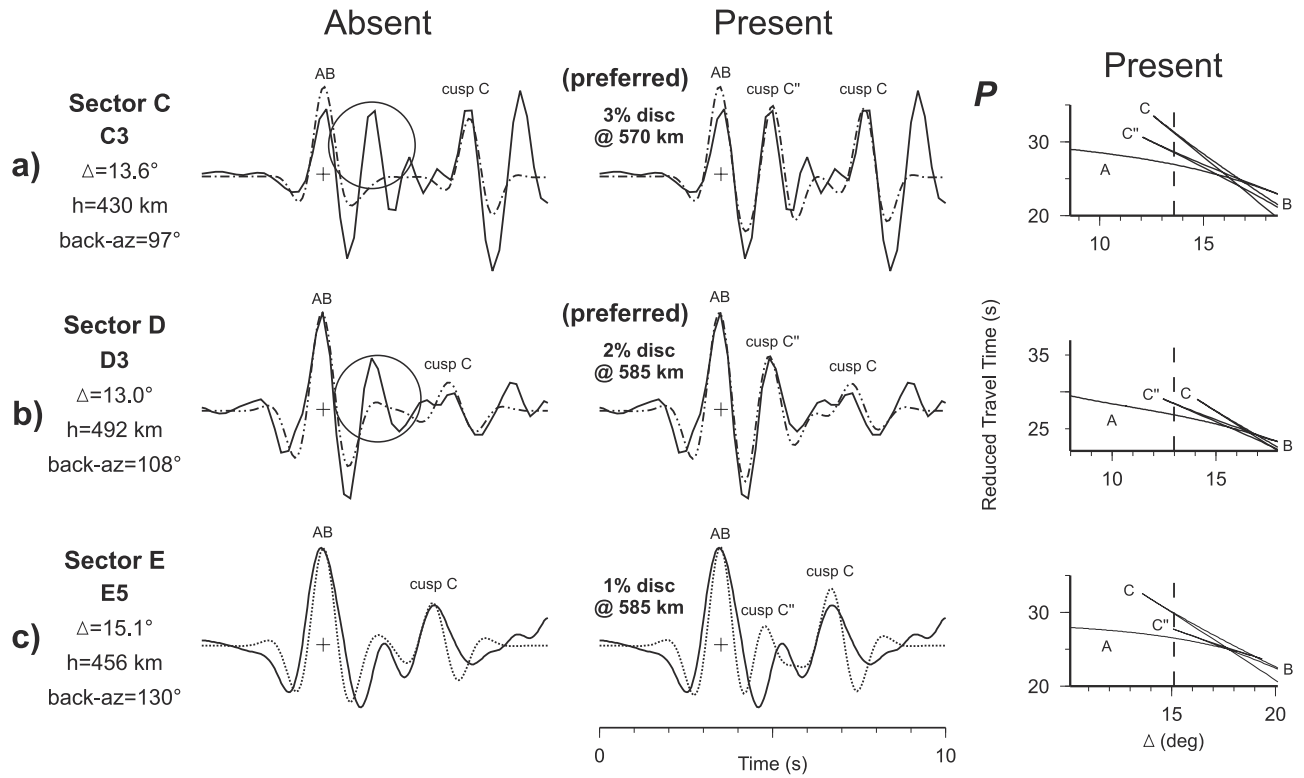
Mid-Transition Zone Discontinuity

Figure B2. Comparisons between observed (solid traces) and synthetic *P* waveforms (dash traces), illustrating the corresponding evidence between V_P and V_S for or against a sizable midtransition zone discontinuity. Layout is the same as Figure B1.
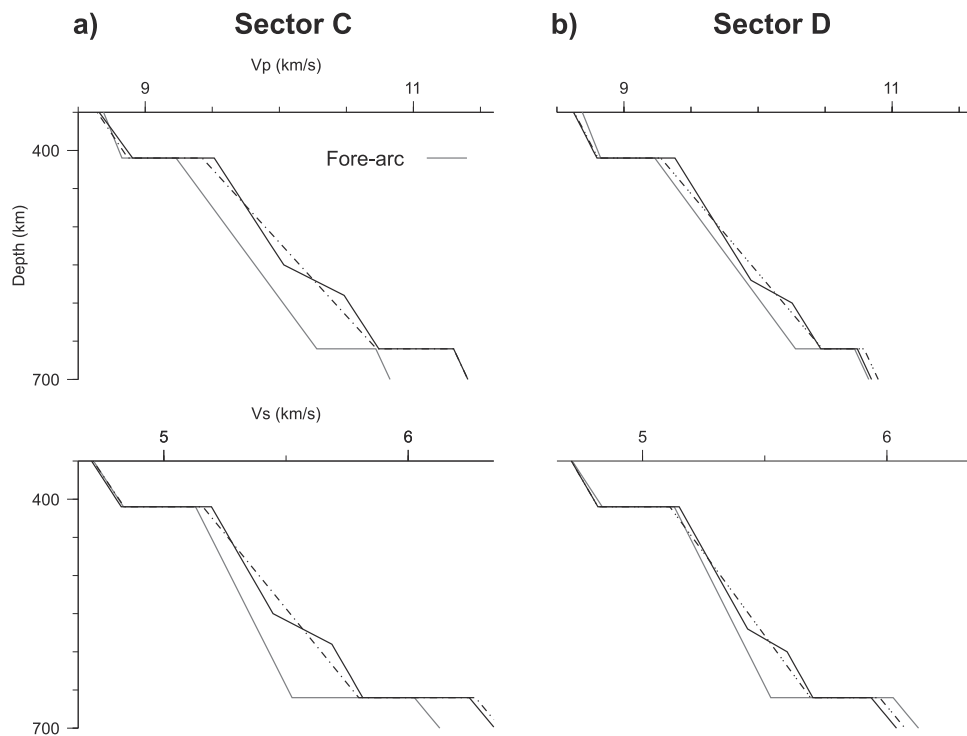

Figure B3. Models for V_P and V_S in sectors C and D, showing cases with or without a midtransition zone discontinuity. Notice that average values of V_P and V_S in the transition zone remain the same in either case, but a single layer of high, linear gradient can be replaced by a 2−3% discontinuity that separates two layers of moderate gradient.

γ phase and that of garnet to Ca-perovskite is $\sim$2% and $\sim$0.5%, respectively [e.g., *Jackson et al.*, 2000; *Sinogeikin et al.*, 1998; *Weidner and Wang*, 2000]. Even a 2% increase from wadsleyite to-ringwoodite is too small to explain a seismic discontinuity much greater than 1.5% in V_P and V_S, unless the mantle has more than 75% olivine. Moreover, such phase changes should occur throughout the Earth, in conflict with observed differences in the size of the discontinuity between sector C ($\sim$3%) and the forearc ($\leq$1%). Thus, phase transitions alone cannot account for a sizable midtransition zone discontinuity.

[71] A clear correlation between a sizable midtransition zone discontinuity and high average values of V_P and V_S in sectors C and D suggest that the two observations share a common cause. In our interpretation, high V_P and V_S in the bottom of the transition zone beneath sectors C and D correspond to a cold aureole of ringwoodite that surrounds a core of metastable olivine in sectors A and B where outboard earthquakes occur (Figure 1). As such, low temperature of the aureole amplifies the effect of phase changes: A 1% increase in V_P and V_S from phase change alone is boosted by another 1−2% due to cold temperature. This interpretation is similar to that of *Oreshin et al.* [1998], who proposed that a gradual increase of V_P and V_S by 2−3% in the middle of the transition zone under eastern Eurasia corresponds to the top of a remnant slab.

[72] Extrapolating from recent laboratory measurements on how V_P and V_S change with temperature [e.g., *Kern*, 1982; *Li et al.*, 1998; *Sinogeikin et al.*, 2001], an increase of 2% in V_P and V_S implies a temperature decrease of 300−600°C. This estimate of moderate temperature contrast is well within the theoretical prediction for a possibly large (>1000°C) thermal contrast between the top and the core of a cold slab like the Tonga WBZ [e.g., *Insergueix et al.*, 1997; *Stein and Stein*, 1996].

[73] In summary, the concept that phase changes must coincide with a subhorizontal anomaly of cold temperature to produce a sizable discontinuity in the middle of the transition zone seems to offer a straightforward explanation for the intermittent nature of such observations and the wide range of depths and sizes of such a discontinuity. A rigorous analysis of this interpretation, however, awaits global characterization of a midtransition zone discontinuity from both seismological and laboratory-based observations.

References

Agee, C. B., and D. Walker, Olivine flotation in mantle melt, *Earth Planet. Sci. Lett.*, 114, 315–324, 1993.

Albaréde, F., and R. D. van der Hilst, New mantle convection model may reconcile conflicting evidence, *Eos Trans. AGU*, 80, 535, 537–539, 1999.

Barazangi, M., B. L. Isacks, J. Oliver, J. Dubois, and G. Pascal, Descent of lithosphere beneath New Hebrides, Tonga-Fiji and New Zealand: Evidence for detached slabs, *Nature*, 242, 98–101, 1973.

Benz, H. M., and J. E. Vidale, Sharpness of upper mantle discontinuities determined from high-frequency reflections, *Nature*, 365, 147–150, 1993.

Bevis, M., et al., Geodetic observations of very rapid convergence and back-arc extension at the Tonga arc, *Nature*, 374, 249–251, 1995.

Billington, S., The morphology and tectonics of the subducted lithosphere in the Tonga-Fiji-Kermadec region from seismicity and focal mechanism solutions, Ph.D. thesis, Cornell Univ., Ithaca, N.Y., 1980.

Bina, C. R., Phase transition buoyancy contributions to stresses in subducting lithosphere, *Geophys. Res. Lett.*, 23, 3563–3566, 1996.

Bock, G., Synthetic seismogram images of upper mantle structure: No evidence for a 520-km discontinuity, *J. Geophys. Res.*, 99, 15,843–15,851, 1994.

Bose, K., and A. Navrotsky, Thermochemistry and phase equilibria of hydrous phases in the system $MgO-SiO_2-H_2O$: Implications for volatile transport to the mantle, *J. Geophys. Res.*, 103, 9713–9719, 1998.

Brudzinski, M. R., and W.-P. Chen, Variations of P wave speeds and outboard earthquakes: Evidence for a petrologic anomaly in the mantle transition zone, *J. Geophys. Res.*, 105, 21,661–21,682, 2000.

Chapman, C. H., A new method for computing synthetic seismograms, *Geophys. J. R. Astron. Soc.*, 54, 481–518, 1978.

Chapman, C. H., J.-Y. Chu, and D. G. Lyness, The WKBJ seismogram algorithm, in *Seismological Algorithms: Computational Methods and Computer Programs*, edited by D. J. Doornbos, pp. 47–74, Academic, San Diego, Calif., 1988.

Chase, C. G., Tectonic history of the Fiji Plateau, *Geol. Soc. Am. Bull.*, 82, 3087–3110, 1971.

Chen, C.-Y., and F. A. Frey, Origin of Hawaiian tholeiite and alkalic basalt, *Nature*, 302, 785–789, 1983.

Chen, W.-P., and M. R. Brudzinski, Evidence for a large-scale remnant of subducted lithosphere beneath Fiji, *Science*, 292, 2475–2479, 2001.

Creager, K. C., and T. H. Jordan, Slab penetration into the lower mantle beneath the Mariana and other island arcs of the northwest Pacific, *J. Geophys. Res.*, 91, 3573–3589, 1986.

Daessler, R., and D. A. Yuen, The metastable olivine wedge in fast subducting slabs: Constraints from thermo-kinetic coupling, *Earth Planet. Sci. Lett.*, 137, 109–118, 1996.

Deuss, A., and J. Woodhouse, Seismic observations of splitting of the mid-transition zone discontinuity in Earth's mantle, *Science*, 294, 354–357, 2001.

Devaux, J. P., G. Schubert, and C. Anderson, Formation of a metastable olivine wedge in a descending slab, *J. Geophys. Res.*, 102, 24,627–24,637, 1997.

Dziewonski, A. M., T.-A. Chou, and J. H. Woodhouse, Determination of earthquake source parameters from waveform data for studies of global and regional seismicity, *J. Geophys. Res.*, 86, 2825–2852, 1981.

Engdahl, E. R., R. D. van der Hilst, and R. P. Buland, Global teleseismic earthquake relocation with improved travel times and procedures for depth determination, *Bull. Seismol. Soc. Am.*, 88, 722–743, 1998.

Faul, U. H., D. R. Toomey, and H. S. Waff, Intergranular basaltic melt is distributed in thin, elongated inclusions, *Geophys. Res. Lett.*, 21, 29–32, 1994.

Fischer, K., K. C. Creager, and T. H. Jordan, Mapping the Tonga Slab, *J. Geophys. Res.*, 96, 14,403–14,428, 1991.

Flanagan, M. P., and P. M. Shearer, Global mapping of topography on transition zone velocity discontinuities by stacking SS precursors, *J. Geophys. Res.*, 103, 2673–2692, 1998.

Frohlich, C., The nature of deep-focus earthquakes, *Annu. Rev. Earth Planet. Sci.*, 17, 227–254, 1989.

Fujisawa, , Elastic wave velocities of forsterite and its spinel form and chemical boundary hypothesis for the 410-km discontinuity, *J. Geophys. Res.*, 103, 9591–9608, 1998.

Glennon, M. A., and W.-P. Chen, Systematics of deep-focus earthquakes along the Kuril-Kamchatka Arc and their implications on mantle dynamics, *J. Geophys. Res.*, 98, 735–769, 1993.

Gossler, J., and R. Kind, Seismic evidence for very deep roots of continents, *Earth Planet. Sci. Lett.*, 138, 1–13, 1996.

Grand, S. P., R. D. van der Hilst, and S. Widiyantoro, Global seismic tomography: A snapshot of convection in the Earth, *GSA Today*, 7, 1–7, 1997.

Green, H. W., II, A graveyard for buoyant slabs?, *Science*, 292, 2445–2446, 2001.

Green, H. W., and P. C. Burnley, A new self-organizing mechanism for deep-focus earthquakes, *Nature*, 341, 733–737, 1989.

Green, H. W., and H. Houston, The mechanics of deep earthquakes, *Annu. Rev. Earth Planet. Sci.*, 23, 169–213, 1995.

Gu, Y., A. M. Dziewonski, and C. B. Agee, Global de-correlation of the topography of transition zone discontinuities, *Earth Planet. Sci. Lett.*, 157, 57–67, 1998.

Hamburger, M. W., and B. L. Isacks, Deep earthquakes in the southwest Pacific: A tectonic interpretation, *J. Geophys. Res.*, *92*, 13,841–13,854, 1987.

Inoue, T., D. J. Weidner, P. A. Northrup, and J. B. Parise, Elastic properties of hydrous ringwoodite (γ-phase) in Mg_2SiO_4, *Earth Planet. Sci. Lett.*, *160*, 107–113, 1998.

Insergueix, D., L. Dupeyrat, M. Menvielle, and E. Tric, Dynamical and thermal structure of a subduction zone: Influence of slab geometry on the convective state of the Earth's upper mantle; preliminary results, *Phys. Earth Planet. Inter.*, *99*, 231–247, 1997.

Isacks, B., and P. Molnar, Distribution of stresses in the descending lithosphere from a global survey of focal-mechanism solutions of mantle earthquakes, *Rev. Geophys.*, *9*, 103–174, 1971.

Isacks, B., J. Oliver, and L. R. Sykes, Seismology and the new global tectonics, *J. Geophys. Res.*, *73*, 5855–5899, 1968.

Ita, J., and L. Stixrude, Petrology, elasticity, and composition of the mantle transition zone, *J. Geophys. Res.*, *97*, 6849–6866, 1992.

Jackson, J. M., S. V. Sinogeikin, and J. D. Bass, Sound velocities and elastic properties of gamma-Mg_2SiO_4 to 873 K by Brillouin spectroscopy, *Am. Mineral.*, *85*, 296–303, 2000.

Karato, S.-I., M. R. Riedel, and D. A. Yuen, Rheological structure and deformation of subducted slabs in the mantle transition zone: Implications for mantle circulation and deep earthquakes, *Phys. Earth Planet. Inter.*, *127*, 83–108, 2001.

Kato, M., and T. H. Jordan, Seismic structure of the upper mantle beneath the western Philippine Sea, *Phys. Earth Planet. Inter.*, *110*, 263–283, 1999.

Katsura, T., and E. Ito, The system Mg_2SiO_4-Fe_2SiO_4 at high pressures and temperatures: Precise determination of stabilities of olivine, modified spinel, and spinel, *J. Geophys. Res.*, *94*, 15,663–15,670, 1989.

Kawamoto, T., K. Leinenweber, R. L. Hervig, and J. R. Holloway, Stability of hydrous minerals in H_2O-saturated KLB-1 peridotite up to 15 GPA, in *Volatiles in the Earth and Solar System*, edited by K. A. Farley, pp. 229–239, AIP Press, New York,, 1995.

Kellogg, L. H., B. H. Hager, and R. D. van der Hilst, Compositional stratification in the deep mantle, *Science*, *283*, 1881–1884, 1999.

Kennett, B. L. N., Seismic Structure and Heterogeneity in the upper mantle, in *Relating Geophysical Structures and Processes: The Jeffreys Volume*, *Geophys. Monogr. Ser.*, vol. 76, edited by K. Aki and R. Dmowska, pp. 53–66, AGU, Washington, D.C., 1993.

Kennett, B. L. N., and E. R. Engdahl, Traveltimes for global earthquake location and phase identification, *Geophys. J. Int.*, *105*, 429–465, 1991.

Kern, S., *P*- and *S*-wave velocities in crustal and mantle rocks under the simultaneous action of high confining pressure and high temperature and the effect of the rock microstructure, in *High-Pressure Researches in Geoscience*, edited by W. Schreyer, pp. 15–45, E. Schweizerbart, Stuttgart, Germany, 1982.

Kirby, S. H., W. B. Durham, and L. A. Stern, Mantle phase changes and deep-earthquake faulting in subducting lithosphere, *Science*, *252*, 216–225, 1991.

Kirby, S. H., E. A. Okal, and E. R. Engdahl, The June 9, 1994 Bolivian deep earthquake: An exceptional event in an extraordinary subduction zone, *Geophys. Res. Lett.*, *22*, 2233–2236, 1995.

Kirby, S. H., S. Stein, E. A. Okal, and D. C. Rubie, Metastable mantle phase transformations and deep earthquakes in subducting oceanic lithosphere, *Rev. Geophys.*, *34*, 261–306, 1996.

Koito, S., M. Akaogi, O. Kubota, and T. Suzuki, Calorimetric measurements of perovskites in the system $CaTiO_3$ - $CaSiO_3$ and experimental and calculated phase equilibria for high-pressure dissociation of diopside, *Phys. Earth Planet. Inter.*, *120*, 1–10, 2000.

Lay, T., The fate of descending slabs, *Annu. Rev. Earth Planet. Sci.*, *22*, 33–61, 1994.

Li, B., R. C. Liebermann, and D. J. Weidner, Elastic moduli of wadsleyite (β-Mg_2SiO_4) to 7 gigapascals and 873 kelvin, *Science*, *281*, 675–677, 1998.

Lithgow-Bertelloni, C., and M. Richards, The dynamics of Cenozoic and Mesozoic plate motions, *Rev. Geophys.*, *36*, 27–78, 1998.

Marton, F. C., C. R. Bina, S. Stein, and D. C. Rubie, Effects of slab mineralogy on subduction rates, *Geophys. Res. Lett.*, *26*, 119–122, 1999.

McGuire, J. J., D. A. Wiens, P. J. Shore, and M. G. Bevis, The March 9, 1994(M_w 7. 6), deep Tonga earthquake; rupture outside the seismically active slab, *J. Geophys. Res.*, *102*, 15,163–15,182, 1997.

McKenzie, D. P., Temperature and potential temperature beneath island arcs, *Tectonophysics*, *10*, 357–366, 1970.

Meade, C., and R. Jeanloz, Deep-focus earthquakes and recycling of water into the Earth's mantle, *Science*, *252*, 68–72, 1991.

Molnar, P., D. Freedman, and J. S. F. Shih, Lengths of intermediate and deep seismic zones and temperatures in downgoing slabs of lithosphere, *Geophys. J. R. Astron. Soc.*, *56*, 41–54, 1979.

Okal, E. A., and S. H. Kirby, Deep earthquakes beneath the Fiji Basin, SW Pacific: Earth's most intense deep seismicity in stagnant slabs, *Phys. Earth Planet. Inter.*, *109*, 25–63, 1998.

Oreshin, S., L. Vinnik, A. Treussov, and R. Kind, Subducted lithosphere or 530 km discontinuity?, *Geophys. Res. Lett.*, *25*, 1091–1094, 1998.

Richards, M. A., and D. C. Engebretson, Large-scale mantle convection and the history of subduction, *Nature*, *355*, 437–440, 1992.

Ryberg, T., F. Wenzel, A. V. Egorkin, and L. Solodilov, Short-period observation of the 520 km discontinuity in northern Eurasia, *J. Geophys. Res.*, *102*, 5413–5422, 1997.

Savage, J. C., The mechanics of deep-focus faulting, *Tectonophysics*, *8*, 115–127, 1969.

Shearer, P. M., Constraints on upper mantle discontinuities from observations of long-period reflected and converted phases, *J. Geophys. Res.*, *96*, 18,147–18,182, 1991.

Silver, P. G., R. W. Carlson, and P. Olson, Deep slabs, geochemical heterogeneity and the large-scale structure of mantle convection, *Annu. Rev. Earth Planet. Sci.*, *16*, 477–541, 1988.

Silver, P. G., S. L. Beck, T. C. Wallace, C. Meade, S. C. Myers, D. E. James, and R. Kuehnel, Rupture characteristics of the deep Bolivian earthquake of 9 June 1994 and the mechanism of deep-focus earthquakes, *Science*, *268*, 69–73, 1995.

Sinogeikin, S. V., T. Katsura, and J. D. Bass, Sound velocities and elastic properties of Fe-bearing wadsleyite and ringwoodite, *J. Geophys. Res.*, *103*, 20,819–20,825, 1998.

Sinogeikin, S. V., J. D. Bass, and T. Katsura, Single-crystal elasticity of γ-$(Mg_{0.91}Fe_{0.09})_2SiO_4$ to 16 GPa and at high temperatures, *Geophys. Res. Lett.*, *28*, 4335–4338, 2001.

Stein, S., and C. A. Stein, Thermo-mechanical evolution of oceanic lithosphere: Implications for the subduction process and deep earthquakes, in *Subduction Top to Bottom*, *Geophys. Monogr. Ser.*, vol. 96, edited by G. E. Bebout et al., pp. 1–17, AGU, Washington, D.C., 1996.

Toomey, D. R., W. S. D. Wilcock, S. C. Solomon, W. C. Hammond, and J. A. Orcutt, Mantle seismic structure beneath the MELT Region of the East Pacific Rise from *P* and *S* wave tomography, *Science*, *280*, 1224–1227, 1998.

van der Hilst, R. D., Complex morphology of subducted lithosphere in the mantle beneath the Tonga trench, *Nature*, *374*, 154–157, 1995.

van der Hilst, R. D., S. Widiyantoro, and E. R. Engdahl, Evidence for deep mantle circulation from global tomography, *Nature*, *386*, 578–584, 1997.

Vidale, J. E., G. Schubert, and P. S. Earle, Unsuccessful initial search for a midmantle chemical boundary with seismic arrays, *Geophys. Res. Lett.*, *28*, 859–862, 2001.

Wadati, K., Existence and study of deep-focus earthquakes (in Japanese), *J. Meterol. Soc. Jpn.*, *Ser.*, *2, 5*, 119–145, 1927.

Weidner, D. J., and Y. Wang, Phase transformations: implications for mantle structure, in *Earth's Deep Interior: Mineral Physics and Tomography From the Atomic to the Global Scale*, *Geophys. Monogr. Ser.*, vol. 117, edited by S. Karato et al., pp. 215–235, AGU, Washington, D.C., 2000.

Wu, L.-R., and W.-P. Chen, Rupture of the large (M_w 7. 8) deep earthquake of 1973 beneath the Japan Sea with implications for seismogenesis, *Bull. Seismol. Soc. Am.*, *91*, 102–111, 2001.

Zhou, H.-W., A high-resolution *P* wave model for the top 1200 km of the mantle, *J. Geophys. Res.*, *101*, 27,791–27,810, 1996.

Zhou, L., W.-P. Chen, and S. Ozalaybey, Seismic properties of the central Indian Shield, *Bull. Seismol. Soc. Am.*, *90*, 1295–1304, 2000.

————————————

M. R. Brudzinski, Department of Geology and Geophysics, University of Wisconsin-Madison, Madison, WI 53719, USA. (brudzins@geology.wisc.edu)

W.-P. Chen, Department of Geology, University of Illinois at Urbana-Champaign, 1301 West Green St - 245 NHB, Urbana, IL 61801, USA. (wpchen@uiuc.edu)